Advancing Passive Microwave Retrievals of Precipitation using CloudSat and GPM Coincidences: Integration of Machine Learning with a Bayesian Algorithm

Reyhaneh Rahimi[a] , Ardeshir Ebtehaj [a] , Lisa Milani [b]

[a] *Department of Civil Environmental and Geo-Engineering and the Saint Anthony Falls Laboratory, University of Minnesota*

[b] *Earth System Science Interdisciplinary Center, University of Maryland - NASA Goddard Space Flight Center*

Corresponding author: Ardeshir Ebtehaj, email@ebtehaj@umn.edu

ABSTRACT: Integration of machine learning with a classic Bayesian algorithm is investigated for passive microwave precipitation retrievals using coincidences from the Global Precipitation Measurement core satellite and the *CloudSat* Profiling Radar (CPR). Among several machine learning models, the eXtreme Gradient Boosting Decision Tree (XGBDT), equipped with a weighted cross entropy loss function, exhibits the highest accuracy in the detection of precipitation occurrence and phase with a true positive rate greater than 94 (98)% and a false positive rate smaller than 1 (1)% for rainfall (snowfall) over land and oceans with no frozen surfaces. Bayesian retrievals in the embedding space of a fully connected multi-layer perception (MLP), equipped with a focal loss function, provide the most accurate estimates of the rates with a mean absolute error of less than 1.80 (0.15) $\mathrm{mm\,hr^{-1}}$ for rainfall (snowfall). Mutual information analysis unravels that beyond the near-surface air temperature, the 37 and 183±7(3) GHz are the most informative channels for phase detection over the ocean (land). The physical consistency of the retrievals and new explanations of the precipitation passive microwave signatures are provided through partial dependence analysis and annual comparison with the reanalysis data.

SIGNIFICANCE STATEMENT: The cloud profiling radar (CPR) onboard the CloudSat satellite provided information about light precipitation and snowfall on a quasi-global scale with unprecedented accuracy for more than 15 years. This study examines how machine learning (ML) and its integration with classic Bayesian statistical approaches can learn from coincidences of CPR and the radiometer onboard the global precipitation measurement (GPM) core satellite to expand our algorithmic tools for a better understanding of precipitation global variability. New approaches are used to interpret the results of the ML model in connection with the underlying physics controlling the precipitation phase change processes and their microwave signatures. Comparisons with observationally constrained simulations from the Earth system models unravel where satellite observations can provide new insights or need further improvements. The outcome paves the way to expand our understanding of the impacts of climate change on snowfall patterns and the hydrologic water cycle.

1. Introduction

Precipitation is monitored remotely from space using passive and active spaceborne instruments in infrared and microwave regions of the electromagnetic spectrum. Microwaves can penetrate the raining clouds and interact with their microphysical properties (Wilheit et al. 1977; Olson 1989). Over the past few decades, the passive microwave (PMW) precipitation retrieval algorithms have advanced along different trajectories depending on the dynamics of surface emissivity over ocean and land.

Over radiometrically cold open oceans, with large-scale variability of surface emissivity, the scatter-free theory of radiative transfer (Wilheit et al. 1977) was used to connect precipitation rates to their emission and absorption properties in low-frequency channels below the oxygen absorption line at 60 GHz. Discrete dipole approximation of the raindrop scattering phase function (Liu and Curry 1992) was employed, and theoretically derived empirical regression equations were used (Kummerow and Giglio 1994; Petty 1994) to retrieve rainfall rates from observations by the Special Sensor Microwave/Imager (SSM/I). The regression approaches evolved into Bayesian retrieval algorithms (Kummerow et al. 1996, 2001; Petty and Li 2013; Kummerow et al. 2015, among others) that rely on offline libraries of a statistically representative number of simulated/observed

brightness temperatures (TB) for computationally efficient inversions of the radiative transfer equation.

Over highly emissive and radiometrically complex land surfaces, simulations of TBs of raining clouds have been challenging due to the uncertainties chiefly related to the quantification of the surface emissivity values. Consequently, the initial algorithms remained predominantly empirical and used thresholding (Grody 1991) and regression models (McCollum and Ferraro 2003) for relating the scattering signatures of precipitation to its rate, using 80–100 GHz channels (Gopalan et al. 2010), with often uncertain outcomes over snow-cover surfaces (Ebtehaj et al. 2016). In parallel to the improvement of active precipitation retrievals over land and oceans (Grecu et al. 2016; Iguchi et al. 2000), Bayesian PMW algorithms used libraries of coincident observations from the precipitation radar and microwave imagers (Petty and Li 2013; Ebtehaj et al. 2015) and reported improved estimates over radiometrically complex surfaces.

Motivated by the launch of the CloudSat (Stephens et al. 2009) and the Global Precipitation Core Satellite (GPM) (Skofronick-Jackson et al. 2017), a body of research was devoted to studying the microwave propagation properties of snowing clouds (Bennartz and Bauer 2003; Skofronick-Jackson et al. 2004; Skofronick-Jackson and Johnson 2011) and characterizing the sensitivity of high-frequency channels to ice aloft and snowfall scattering. Radiative transfer modeling and ancillary forecast data were utilized to implement Bayesian algorithms for snowstorm retrievals using the Advanced Microwave Sounding Unit (AMSU) high-frequency TBs (Noh et al. 2006; Kim et al. 2008).

Liu and Seo (2013) demonstrated that snowfall high-frequency scattering could be masked by the emission of supercooled liquid water content in snowing clouds and called for empirical approaches that rely on coincident observations from CloudSat. Kongoli et al. (2003) utilized empirical thresholding of low and high-frequency AMSU channels for global snowfall retrievals over snow-free land surfaces. Hybrid algorithms were proposed (Kongoli et al. 2015; You et al. 2022) that used logistic regression and iterative inversion of a one-layer two-stream radiative transfer model (Meng et al. 2017) using the Advanced Technology Microwave Sounder (ATMS) data. Despite substantial progress, comparisons of satellite retrievals of high-latitude precipitation and reanalysis data (Munchak and Skofronick-Jackson 2013; Behrangi et al. 2016; You et al. 2023) uncovered that PMW satellite snowfall data are still highly uncertain, especially over radiometrically complex

ice sheets (Milani et al. 2018), snow-covered lands (Rahimi et al. 2022) and those areas affected by extreme moisture transport from large inland lakes (Milani et al. 2021).

Modern PMW retrieval algorithms have emerged to utilize machine learning (ML) advances (Tapiador et al. 2004). In one of the early attempts, Sanò et al. (2018) trained a shallow neural network for rainfall retrievals, using coincidences (Grecu et al. 2016) of the GPM Microwave Imager (GMI) and the GPM dual-frequency precipitation radar (DPR). The algorithm was further expanded for snowfall retrievals using GMI and CloudSat coincidences based on a random forest (RF) (Rysman et al. 2018) and later on using an XGBDT for estimation of the rates (Rysman et al. 2019). Similarly, Tang et al. (2018) proposed a fully connected neural network with two hidden layers and trained it, chiefly using coincidences of GMI, DPR, and CPR data, for high-latitude rain and snowfall retrievals.

Unlike pixel-level ML models, Gorooh et al. (2022) used a U-Net architecture (Ronneberger et al. 2015) for rainfall retrieval using both GPM and geostationary infrared spatial data. Orescanin et al. (2021) deployed a Residual Network (ResNet, He et al. 2016) to distinguish convective precipitation using the GMI-DPR coincidences. Pfreundschuh et al. (2022) expanded the Bayesian Goddard Profiling Algorithm (Kummerow et al. 2015) using quantile regression convolutional neural networks (Taylor 2000). More recently, a convolutional neural network (Bannai et al. 2023) was proposed that used a weighted average of cross entropy and mean squared error (mse) loss functions for one-step PMW precipitation retrievals using GPM and DPR coincidences.

This paper extends the previous research through the following contributions using the latest version of CloudSat and GPM satellite coincidences (Turk et al. 2021). (i) The paper presents a two-step PMW retrieval framework and examines it for precipitation occurrence and phase detection (step 1) and rate estimation (step 2). The phase determination does not rely on thresholding based on the near-surface air temperature and uses it as an input. (ii) Different pixel-level ML models including random forests (Breiman 2001), XGBDT (Chen and Guestrin 2016), and MLP are tested and compared. Although convolutional neural networks (CNNs) have shown some success with limited horizontal coverage in other studies (Amell et al. 2024), we excluded CNNs here due to the minimal spatial overlap in GMI-CPR coincidences, which further restricts the spatial context needed for CNNs to perform effectively in this framework. (iii) A new precipitation rate estimation framework is proposed by conducting Bayesian PMW retrievals in the embedding space of an MLP

that reduces the uncertainty of rate estimation beyond the deployed off-the-shelf ML algorithms using proper reflectivity (Z) to rainfall rate (R) or snowfall rate (S) relationships. (iv) The causal relationships between TBs and precipitation occurrence and phase change are unveiled through explainable ML using mutual information (Peng et al. 2005) and partial dependence analyses (Hastie et al. 2009).

The paper is organized as follows. Section 2 describes the data, and the methodology is explained in Section 3. The results, findings, and discussions are presented in Section 4. Section 5 provides a summary and points out future research directions.

2. Data sets

a. Satellite coincidences and ancillary data

This study uses the latest version of near-coincident GMI brightness temperatures with CPR (DPR) active retrievals (2B-CSATGPM) from March 2014 to August 2019 (January 2021 to December 2022) – the last date reported by the CloudSat data processing center (personal communication with Dr. J. Turk at Jet Propulsion Laboratory, Turk et al. 2021) as well as the ERA5 reanalysis data (Hersbach et al. 2018). The precipitation products and land surface types from the Goddard Profiling Algorithm (GPROF, Kummerow et al. 2015, V07) are also used for cross-comparisons and assessments. It should be noted that the surface type used by GPROF is carried within the GPM-CloudSat dataset.

The CPR near surface snowfall data are from the latest level-II products including the 2C-PRECIP-COLUMN (Haynes et al. 2009) and the 2C-SNOW-PROFILE (Wood et al. 2013, 2014) that contain the information related to precipitation phase and snowfall rate, respectively. To avoid ground-clutter contamination, the near-surface rates within radar bins above the oceans (land) at 720 m (1200 m) height (Kulie et al. 2010) are used. Note that overland rainfall retrievals are unavailable for CloudSat products. Even though the CPR-based snowfall retrievals are central to the goal of the paper, for the sake of completeness, the near-surface rainfall data from 2A-DPR Ku-band product (Iguchi et al. 2018), based on blind zone extrapolations (Hirose et al. 2021; Shimizu et al. 2023), are used to train the algorithm and present the results for a multiclass precipitation phase detection. Note that the DPR precipitation phase is determined via a combination of the bright band detection algorithm evaluation of the atmospheric temperature profile (Iguchi et al.

2018). Meanwhile, CloudSat 2C-PRECIP-COLUMN uses the estimated height of the melting layer from the European Centre for Medium-Range Weather Forecasts (ECMWF) reanalysis and models for expected snow particle melting to distinguish snow from rain (Wood et al. 2014).

It is worth noting that, unlike the CPR, research suggested that DPR is not sufficiently sensitive in capturing backscattering signatures of light precipitation (Liu 2008; Hamada and Takayabu 2016) with rates less than 0.2–0.5 mm hr^{-1} (Skofronick-Jackson et al. 2013; You et al. 2017; Casella et al. 2017). At the same time, it is essential to highlight that for intense storms, the CPR reflectivity tends to saturate near 20 dBZ as the size of the hydrometeors approaches the wavelength (Matrosov and Battaglia 2009; Liu 2008). This saturation often increases the uncertainty of the retrievals as the precipitation intensity grows (Lécuyer and Stephens 2002; Tang et al. 2017).

b. Training and validation data sets

We use imbalanced data for training, validation, and testing based on the available coincidences. The dataset for training and validation was randomly permuted and split into 70% for training and 30% for validation. The test set was constructed using independent data from the final year of each overlap period, with January 2021 to December 2021 for GMI-DPR and July 2018 to August 2019 for GPM-CloudSat. To construct our training and testing data sets, we confine our considerations to the GMI and DPR (CPR) rainfall (snowfall and clear sky) coincidences. For snowfall data, we utilize DPR data only for heavy rates where CPR is likely to saturate with reflectivity values greater than 15–20 dBZ (Matrosov and Battaglia 2009). Using Z-S relationship by Liu (2008), this reflectivity range translates into 2.2–5.6 mm hr^{-1}. To alleviate this issue, we use DPR snowfall when CPR snow rates are ≥ 4 mm hr^{-1}, constituting only a small fraction of data points.

The training data is augmented by the ERA5 2-m air temperature (T2m), water vapor path (WVP), cloud liquid (LWP), and ice (IWP) water paths as well as convective available potential energy (CAPE). The data are stratified only based on five different surface types including open oceans, sea ice, land surfaces with no snow, snow cover, and coastal zones through agglomerating the dynamic surface types provided by the Goddard Profiling Algorithm (GPROF, Kumerrow 2016).

The number of coincidences differs over the surface types due to their spatial extent and satellite coverage. We use an imbalanced representation of rain, snow, and clear sky classes across each surface type to train the ML classification algorithms to ensure unbiased retrievals. A summary

Surface type	Ocean	Land	Coast	Sea ice	Snow cover
# imbalanced samples	3.4E+6	1.8E+6	5E+5	4.1E+5	3.3E+5

TABLE 1. The total number of imbalanced data points over five different surface types used for training and testing.

of the number of available coincidences is reported in Tab. 1. Probability histograms of the training data are also shown over three grouped surface types in Fig. 1. The DPR rainfall rates are positively skewed over all surfaces with a global mean of around 1.7 $\mathrm{mm\,hr^{-1}}$. The distribution of CPR snowfall rates is much wider than the DPR rainfall distribution and has a significantly smaller global mean value ~0.3 $\mathrm{mm\,hr^{-1}}$. While the tail of the rainfall distributions extends to almost 20 $\mathrm{mm\,hr^{-1}}$, the bulk of the snowfall density is accumulated below 2 $\mathrm{mm\,hr^{-1}}$.

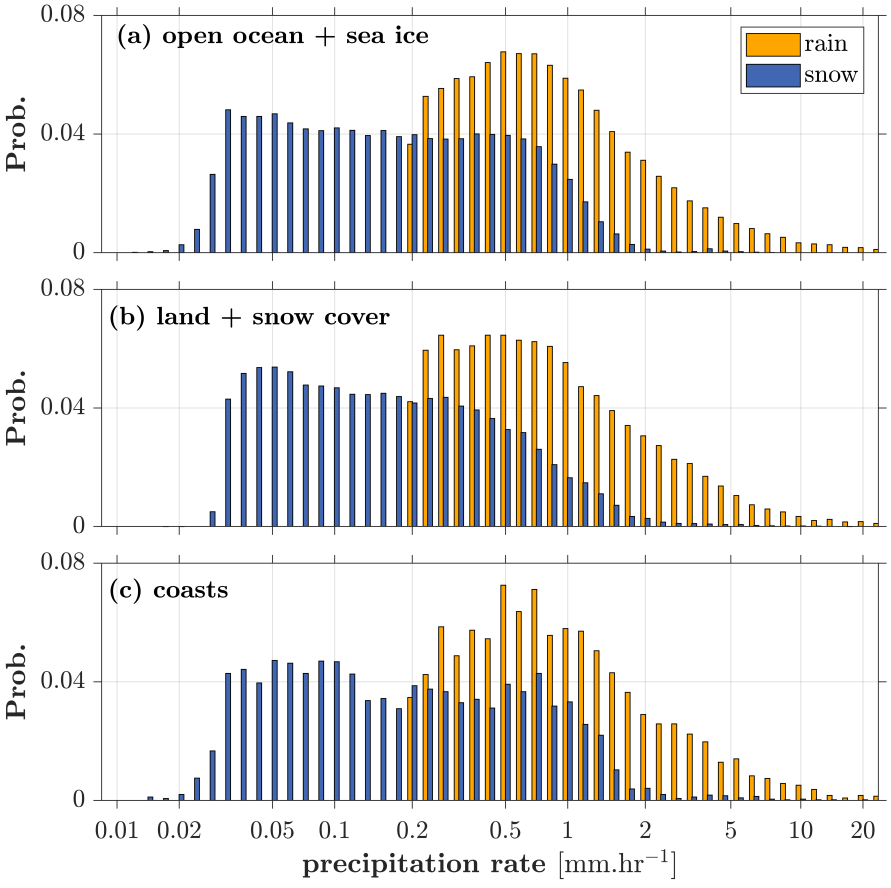

FIG. 1. Probability histograms of the rainfall and snowfall data over three grouped surface types as explained in the text.

3. Methodology

a. Retrieval algorithm

In the first phase of the algorithm, a classification model detects the occurrence and phase of precipitation, given pixel-level inputs of TBs and the ERA5 physical precipitation drivers. In the second step, a regression model estimates the rate of precipitating pixels. We take a two-step approach mainly because optimal classification and regression loss functions can be deployed separately. The regression network with a regression loss function often leads to a lower detection accuracy than those equipped with classification loss functions. Moreover, a two-step paradigm allows phase detection and does not require thresholding using near-surface air temperature values. Thus the algorithm can be trained for different snowfall and rainfall *Z*-*S*, and *Z*-*R* relationships.

As previously explained, for the phase detection, over each surface type, a set of classic machine learning algorithms are examined including *k*-nearest neighbors (*k*NN, Cover and Hart 1967), random forest (RF, Breiman 2001), XGBDT (Chen and Guestrin 2016), and a deep multi-layer perception (MLP) (Atkinson and Tatnall 1997). For the estimation step, we implement a Bayesian algorithm called the shrunken locally linear embedding algorithm for retrieval of precipitation (ShARP, Ebtehaj et al. 2015) in the feature of an MLP.

1) Detection step

We employ the same procedure for using the *k*-nearest neighbor for PMW precipitation retrievals in a Bayesian setting as explained in (Ebtehaj et al. 2015, 2020) with the number of nearest neighbors ranging from 10–30. All machine learning models in the detection step are trained based on the weighted cross entropy (Wang et al. 2020). The weighted cross entropy loss accounts for the effects of imbalanced labels as the number of rain and snowfall labels is much smaller than the clear sky cases. This loss function for a multi-class classification can be expressed as follows:

$$\mathcal{L}(\mathbf{x}_i, \boldsymbol{\theta}) = -\sum_{i=1}^{N} \alpha_i y_i(\mathbf{x}_i) \log \hat{y}_i(\mathbf{x}_i), \tag{1}$$

where α_i is the imbalance parameter, y_i is the one-hot encoding of the labels of input features $\mathbf{x}_i$, $\hat{y}_i$ is the ML predicted probability of y_i, and $\boldsymbol{\theta}$ denotes the trainable parameters of the ML. Since

the training set is imbalanced towards clear-sky data points, improved detection is expected when $\alpha_i > 1$ is assigned for rain and snowfall classes.

We use an exhaustive grid search approach (Bergstra and Bengio 2012) for the hyperparameter tuning of the ML models. In particular, the RF and XGBDT are tuned for the number of estimators (i.e., 100–300), maximum tree depth (i.e., 15–30), and minimum sample split number (i.e., 2–10). Additionally, the learning rate, ranging from 0.01 to 0.3, is optimized for XGBDT. The architecture of the MLP for detection features six layers with Rectified Linear Units (ReLU) and a 15% dropout which is trained using the Adam algorithm (Kingma and Ba 2014). The batch size (i.e., 1024), the initial learning rate (i.e., 0.001), and the number of neurons (i.e., 50) are optimized through a random grid search approach.

The optimal imbalance weights α_i are obtained through additional exhaustive hyperparameter tuning based on the maximization of the F1-score. Conceptually, larger values of α increase the true positive rate (TPR) or recall TP/(TP+FN) but decrease precision TP/(TP+FP), where TP, FN, and FP are the true positives, false negatives, and false positives. Selecting an appropriate α to maximize the F1-score (i.e., the harmonic mean of the precision and recall) ensures a balance between precision and recall. Our analysis shows that the effects for different choices of α in the F1-score are uniform across the used ML models and land surface types. We conducted several hyperparameter tuning experiments and assigned optimal weights of 5 (snowfall), 2 (rainfall), and 1 (clear sky) in Eq. 1.

2) Estimation step

For using the ML models in the estimation step, we only change their penalty functions to a least-squares regression loss function and train them based on active retrievals using proper *Z-R* and *Z-S* relationships. As will be shown later, in the detection phase, XGBDT and MLP provide comparable results; however, the former indicates marginally superior performance, especially for surface types with a smaller number of samples (e.g., sea ice). In the estimation phase, we realized that on average, the mean-squared of the MLP is greater than XGBDT appreciably for rainfall and snowfall over different land surface types. We conjecture that the training sample size is the main contributing factor, as neural networks often need a large sample size, especially for imbalanced data with skewed distribution. This is consistent with recent research showing that for tabular

or pixel-level data, the gradient-boosting decision trees provide state-of-the-art results beyond the most advanced deep learning methods (Borisov et al. 2024). However, as will be presented later, a classic Bayesian algorithm in the embedding space of the MLP can provide the most accurate estimation of precipitation rates over most of the surface classes.

To that end, the Bayesian Shrunken locally linear embedding Algorithm for Retrieval of Precipitation (Ebtehaj et al. 2015) is implemented in the embedding space of the MLP, hereafter called ShARP$^{\mathrm{ML}}$. This model comprises four fully connected layers, each containing 75 neurons and utilizing the ReLU activation function. We discretize the precipitation rates and recast the rate estimation into a multi-class classification problem. This formalism enables the network to learn the features associated with the entire probability distribution of precipitation rather than those that can be encoded solely through a least-squares minimization. However, the defined precipitation rate classes are significantly imbalanced due to the positive skewness of the precipitation distribution and a continuous retrieval is infeasible.

To alleviate the class imbalance problem, we use the focal loss, $F_L(p,q) = -\sum_{x\in X}\eta(x)\,[1-q_X(x)]^{\gamma}\,p_X(x)\log q_X(x)$, in which $p_X(x)$ and $q_X(x)$ are distributions of observed and predicted class probabilities, respectively. This loss function modifies the cross-entropy in two ways. First, the parameter η balances the weights of the loss associated with each class, which is set to the inverse of the frequency of the within-class sample size. Second, as the modulating factor $\gamma > 0$ increases, it amplifies the impacts of low-probability classes in the total loss with recommended values of $\gamma = 2$ to 5. Here η is chosen based on the frequency of the different classes and the $\gamma = 2$.

The pre-trained network maps the inputs onto a lower-dimensional embedding space that feeds the Bayesian retrieval algorithm for obtaining continuous retrievals. By the embedding space, here we mean the outputs of the last fully connected $(l-1)^{\mathrm{th}}$ layer of the pre-trained MLP that is $\mathbf{z} = \mathcal{F}^{l-1}(\mathbf{x}) \in \mathbb{R}^{n_f}$, where $n_f = 10$ represents the number of neurons in the last layer and $\mathbf{x} \in \mathbb{R}^{18}$ represents the dimension of inputs consisting 13 TB channels and 5 ERA5 variables.

In particular, let us assume that M vectors of input predictors $\mathbf{x}_i \in \mathbb{R}^n$ and their corresponding precipitation rates $\mathbf{r}_i$ are collected in a database $\mathcal{B} = \{(\mathbf{x}_i, \mathbf{r}_i)\}_{i=1}^{M}$, which is transformed into the embedding space as $\mathcal{B}_f = \{(\mathbf{z}_i, \mathbf{r}_i)\}_{i=1}^{M}$ – using the pre-trained MLP. For a given observed predictor $\mathbf{x}_j^o$, we can obtain its counterpart in the embedding space, $\mathbf{z}_j^o = \mathcal{F}^{l-1}(\mathbf{x}_j^o) \in \mathbb{R}^{n_f}$ and then use

the Bayesian model to retrieve the precipitation rate. Specifically, for each $\mathbf{z}_j^o$, its k-nearest-neighbors $\{\mathbf{z}_k\}_{k=1}^K$ and their corresponding rates $\{\mathbf{r}_k\}_{k=1}^K$ are isolated in $\mathcal{B}_f$ to retrieve the rate as $\hat{\mathbf{r}}_j = \sum_{k=1}^K w_k \mathbf{r}_k$.

To calculate the weights w_k, we employ a ridge regression: $\|\mathbf{z}_j^o - \mathbf{Z}_k\mathbf{w}\|_2^2 + \lambda\|\mathbf{w}\|_2^2$ such that $\sum_k w_k = 1$, $w_k > 0$. Here, $\|\cdot\|_2^2$ is the 2-norm, $\mathbf{Z}_k \in \mathbb{R}^{n_f \times K}$ denotes a matrix containing $\{\mathbf{z}_k\}_{k=1}^K$ in its column space, $\mathbf{w} \in \mathbb{R}^K$ is a vector representation of weights, and $\lambda > 0$ represents a regularization parameter, which is set to 0.01 through cross-validation. One of the important features of the ShARP$^{\text{ML}}$ is that the statistics (e.g., variance, quantiles) of $\{\mathbf{r}_k\}_{k=1}^K$ can provide an uncertainty bound around $\hat{\mathbf{r}}_j$.

b. Explainable machine learning

Two key questions often emerge for ML-based PMW retrieval of precipitation. What are the most important predictors? Can ML capture the expected underlying governing physical laws? To shed light on these questions, we employ the maximum relevance and minimum redundancy (MRMR, Peng et al. 2005) and the partial dependence (PD) analysis (Hastie et al. 2009).

1) Minimum redundancy and maximum relevance

The MRMR method uses mutual information to identify the most informative and the least redundant features among the predictors irrespective of the ML algorithm. Specifically, it finds an optimal set of predictors $\mathcal{S}$ that maximizes the relevance $A_\mathcal{S} = 1/|\mathcal{S}| \sum_{x\in\mathcal{S}} I(x,y)$ to the response variable with minimum internal redundancies $B_\mathcal{S} = 1/|\mathcal{S}|^2 \sum_{x,z\in\mathcal{S}} I(x,z)$, where $I(\cdot,\cdot)$ is the mutual information and $|\mathcal{S}|$ denotes the cardinality of $\mathcal{S}$. The MRMR method computes the Mutual Information Quotient (MIQ) for each predictor outside the selected set $\mathcal{S}^c$, by maximizing the ratio of its relevance to the response variable over the average redundancy with the selected features. This is mathematically expressed as $\max_{x\in S^c} MIQ_x = \max_{x\in S^c} \frac{I(x,y)}{\frac{1}{|S|}\sum_{z\in S} I(x,z)}$.

2) Partial dependence analysis

The PD analysis offers interpretability of the relationship between the input predictors $\mathbf{x}_i$ and the response of an ML model $f(\cdot)$. To that end, for a set of m predictors $\mathbf{X} = \{\mathbf{x}_i\}_{i=1}^m$, the approach computes the dependency of a response to $\mathbf{x}_i$ by marginalizing over the complement

set $\mathbf{X}^{C_i} = \mathbf{X} - \{\mathbf{x}_i\}$ as $g(\mathbf{x}_i) = \int f(\mathbf{x}_i, \mathbf{X}^{C_i}) p_C(\mathbf{X}^{C_i}) d\mathbf{X}^{C_i}$, where $p_C(\mathbf{X}^{C_i})$ denotes the probability distribution of $\mathbf{X}^{C_i}$.

4. Results and Discussion

The results are shown and discussed in four steps. First, we show the performance metrics of classification and estimation steps for the testing data sets. Second, the results of explainable ML are presented. Third, orbital retrievals of a few snowstorms over Greenland and the North Atlantic Ocean are presented. Lastly, we provide the annual retrievals for all GMI orbits in the year 2022 and compare them with the current official GPM product and ERA5 reanalysis data. We need to emphasize that the comparisons with the GPROF product are subjective as the algorithms are different and use fundamentally different training data sets.

a. Detection quality metrics

Figure 2 shows the TPR (TPR = TP/TP+FN) and false positive rates (FPR = FP/FP+TN) over different surface types, where TN denotes true negatives. The *k*NN has the lowest performance for rainfall detection (Fig. 2a), across all land surface types. Typically, when the training sample size is sufficiently large, the MLP slightly outperforms the decision trees; however, based on the available training sample sizes, the XGBDT exhibits the highest overall performance across most surface types. Specifically, the TPR in rainfall detection over the ocean (land) is around 94 (95)% for MLP and XGBDT (Fig. 2a). However, the XGBDT reduces the false alarm rate from around 3 (2)% in MLP over the ocean (land) to around 1%. Over the coasts, both decision tree-based models outperform the MLP with higher (lower) TPR (FPR) values of 2–3 (1–3)%.

For the snowfall detection (Fig. 2b), the *k*NN shows the lowest TPR over all surface types. The XGBDT performs the best consistently almost over all surface types, except coastal regions, with a TPR greater than 95% and an FPR below 2%. Overall, the mean TPR values among different ML models are larger for snowfall than rainfall detection by almost 5%, while the FPR values are approximately the same. Additionally, we compare the F1-score of all ML approaches. Once again, XGBDT consistently shows the highest F1-score across all land surface and precipitation types as shown in Fig. 3. Therefore, we use XGBDT for the detection step.

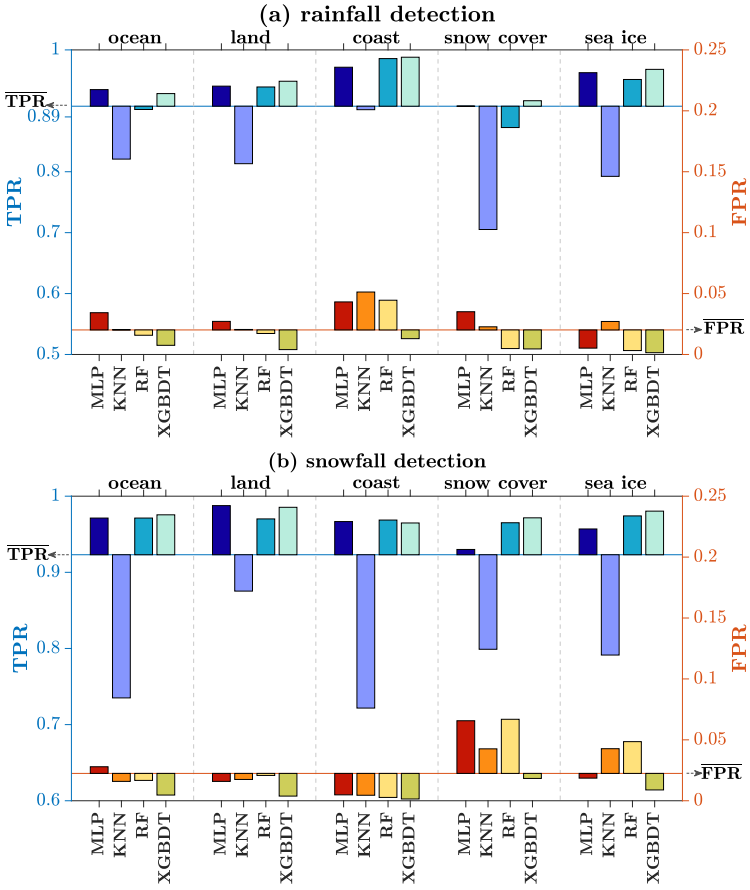

301 FIG. 2. The true (TPR) and false positive rate (FPR) of rainfall (top) and snowfall (bottom) detection using four
302 different ML classification models over different surface types, where the $\overline{\text{TPR}}$ and $\overline{\text{FPR}}$ represent the average
303 values across all models.

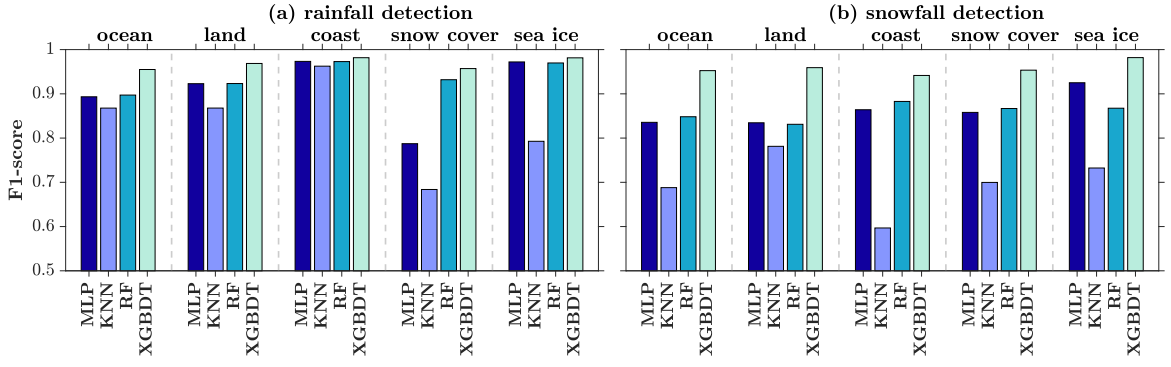

321 FIG. 3. F1-score of rainfall (left) and snowfall (right) detection using four different ML classification models
322 over different surface types.

TABLE 2. Conditional root mean square error (rmse, $\mathrm{mm\,hr^{-1}}$) of ShARP$^{\mathrm{ML}}$ and XGBDT for estimation of precipitation rate, given the occurrence and phase are determined in the detection step.

			Surface Type				
			ocean	land	coast	snow cover	sea ice
rain	rmse	ShARP$^{\mathrm{ML}}$	2.70	2.23	3.01	0.57	0.45
		SHARP	3.20	2.82	3.15	0.65	0.44
		XGBDT	2.90	2.92	3.10	0.58	0.43
snow	rmse	ShARP$^{\mathrm{ML}}$	0.21	0.21	0.20	0.18	0.17
		SHARP	0.26	0.28	0.32	0.24	0.24
		XGBDT	0.32	0.36	0.31	0.19	0.16

A comparison of the results with some previous works is not straightforward because of the lack of non-uniform training and testing data sets. For example, the training data in (Pfreundschuh et al. 2022) differ notably as they utilized ERA5 precipitation over sea ice, compensating for limitations in DPR-based reference retrievals. Additionally, collocations of ground-based radar data were employed over snow-covered surfaces in their analysis. The All-Surface Snow Water Path Retrieval Algorithm (SLALOM, Rysman et al. 2018) used the random forest and trained it using an older version of GMI-CPR coincidences (Turk et al. 2021). The highest values of 83% (TPR) and 12% (FPR) were reported over land, open sea, and sea ice. The reported improvements can be attributed to the following reasons. (i) The latest version of CPR and GMI coincidences include more crossings than the older version. (ii) The XGBDT is used rather than RF, which uses a different parameterization. (iii) We are using weighted cross-entropy loss to formally account for the imbalanced nature of the training and testing data sets.

b. Estimation quality metrics

Table 2 compares the performance of ShARP$^{\mathrm{ML}}$ and XGBDT in the estimation step in terms of the conditional root mean square error (rmse, $\mathrm{mm\,hr^{-1}}$), given that the precipitation occurs. The two models have comparable skills; however, ShARP$^{\mathrm{ML}}$ outperforms the XGBDT over the oceans and land. Conversely, over coastal, snow cover, and sea ice surfaces with relatively small training sample sizes; the XGBDT is still marginally the best choice. Additionally, Table 2 presents the performance of the original SHARP algorithm (Ebtehaj et al. 2015) showing lower skills compared to the ShARP$^{\mathrm{ML}}$ model.

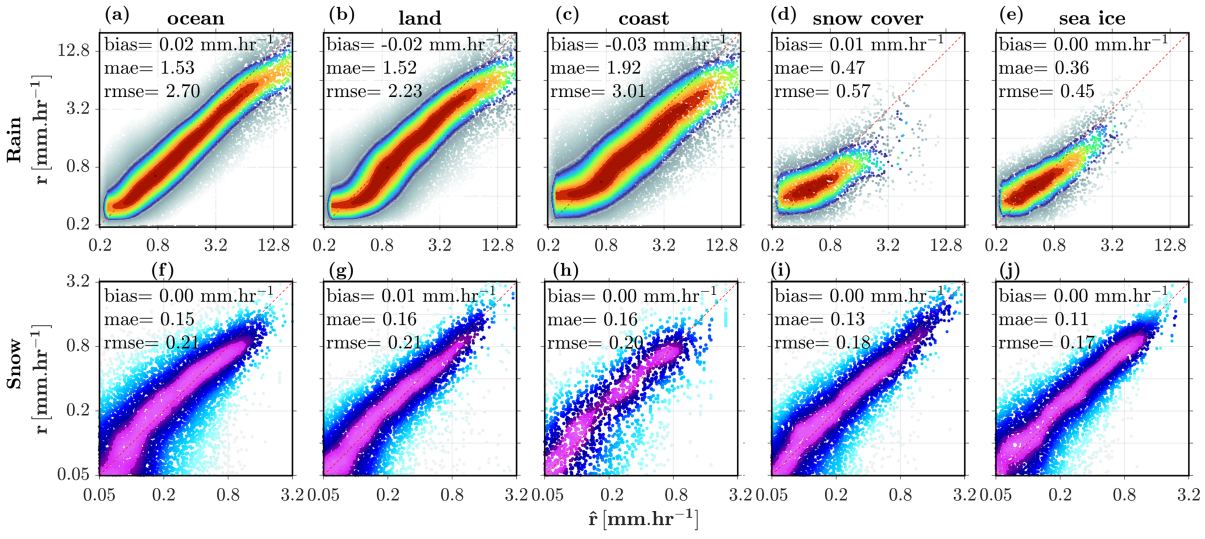

FIG. 4. Density scatter plots of conditional retrievals of rainfall (a–e) and snowfall (f–j) rates by the ShARP^{ML} for the test data. The quality metrics are biases, root mean square errors (rmse), and mean absolute errors (mae). The scatter plots are normalized column-wise for improved visualization and the color of the scatter plots captures the relative density of the points from blue to red (rainfall) rain and magenta (snowfall).

The ShARP^{ML} results, with $K = 20$ nearest neighbors, are presented in Fig. 4 for both rainfall (top row) and snowfall (bottom row) test data, given that the precipitation and its phase are detected. The bias is relatively under control and is larger for rainfall than snowfall. The light (heavy) rainfall rates are overestimated (underestimated), especially over those surface types with limited sample sizes. This is a generic pattern when an unbiased estimator attempts to retrieve data with a positively skewed distribution. This gives rise to small negative biases as the algorithm struggles to retrieve the heavy rainfall rates, especially over surface types with limited training samples. The rmse values of conditional retrievals and their gaps with their mean absolute error (mae) counterparts are larger for rainfall than snowfall over most land cover types, due to the heavier tail probability distribution of rainfall. The mean mae values of rainfall (snowfall) amongst all land surface types is around 1.15 (0.14) mm hr^{-1}. The largest rmse is related to rainfall retrievals over coastal areas and snowfall over land and oceans. The large rmse can be attributed to the small sample size for the coastal rainfall. At the same time, the heaviest convective rainfall (snowfall) occurs over land (oceans) and contributes to the observed elevated error statistics.

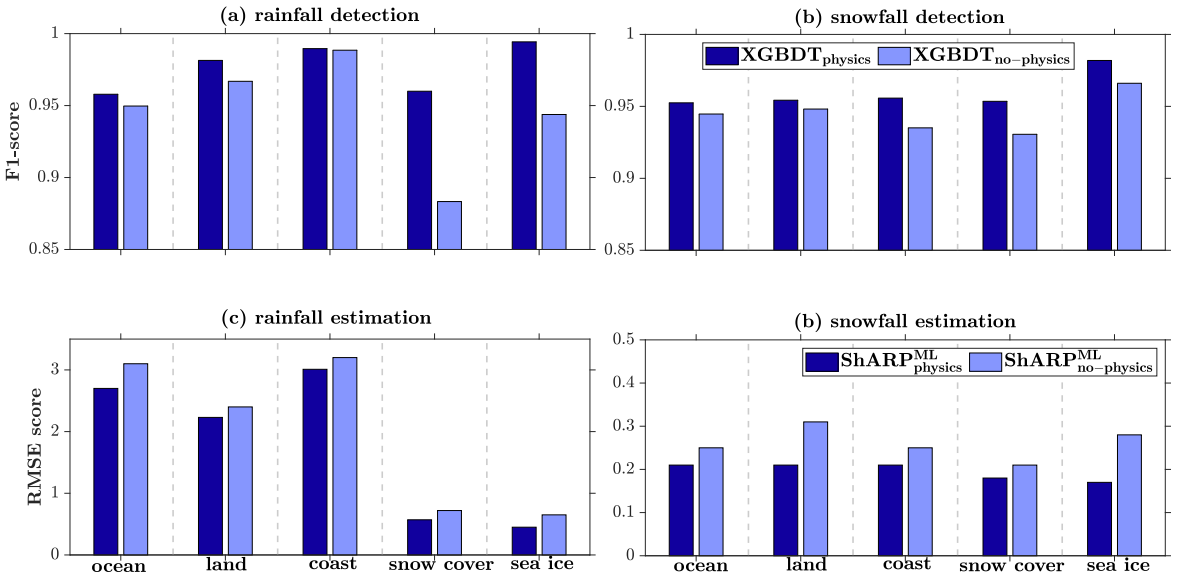

FIG. 5. The effects of ERA5 physical variables on detection (a–b), and estimation (c–d) performance of final retrieval models.

c. Impacts of the Reanalysis Physical Variables

Figure 5 highlights the effect of incorporating physical variables from ERA5 on the detection and estimation capabilities of XGBDT and ShARP$^{\text{ML}}$ models across various surface types. As is evident, the F1-score increases across all land surface types for both rain and snowfall detection. This increase seems marginal and less than 2% over ocean and land for both rain and snow. However, we need to recall that each GMI orbit consists of 221×2961 number of pixels. Therefore, on an annual basis, only a 1% improvement in the F1-score translates into more than 10 million pixel-level events, considering 30% of each orbit is precipitating. The impact on the rmse values is also significant. On average, the rmse values decrease by 15 (9)% over ocean (land) for rainfall and 14 (33)% for snowfall.

d. Interpreting the ML results

For brevity, we confine our considerations to the data points collected only over ocean and land surface types to investigate mutual information of the inputs with precipitation occurrence and phase change and the consistency of the detection module with the underlying physical causalities.

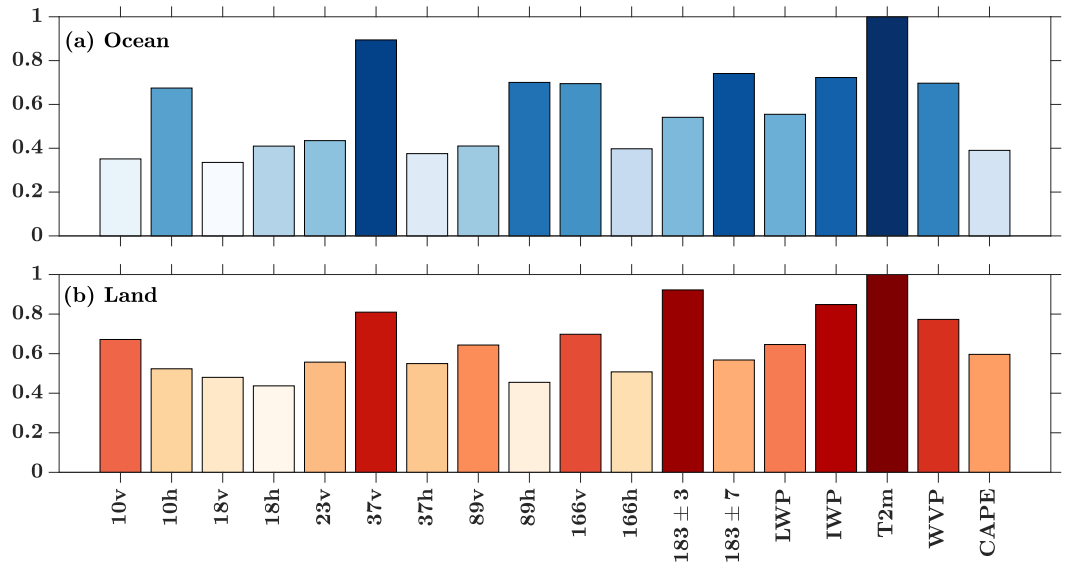

FIG. 6. Mutual Information Quotient (MIQ) derived from Minimum Redundancy Maximum Relevance (MRMR) analysis for inputs used in precipitation and its phase detection over the ocean (a) and land (b). Darker shades represent higher MIQ values, indicating greater importance of the corresponding features.

1) MRMR

The results of MRMR analysis (Fig. 6) show that, amongst the input variables, the 2-m air temperature is the most important one for the classification of the atmosphere into a clear, raining, and snowing atmosphere both over land and ocean, which is simply consistent with our physical understanding of precipitation phase change. The other two most important inputs are the liquid water and the water vapor channels at 37v and 183 GHz followed by ice scattering at 166v GHz.

It is well understood that the total columnar atmospheric liquid water content increases the absorption at 37 GHz. This channel has been widely used for rain and cloud liquid water retrievals over oceans (O'Dell et al. 2008). The overland MRMR importance of 37v is surprising as it does not capture a strong emission/scattering signal of liquid water particles over highly emissive surfaces. The importance of this channel might be interpreted in light of its relationship with land surface temperature (Holmes et al. 2009). The MRMR analysis is performed separately on snow-clear, rain-clear, and snow-rain label cases for testing this conjecture. The results (not shown here), revealed that when considering only snow-clear and rain-clear labels, the MRMR score drops from 0.8 to 0.4. In other words, the 37v channel provides no relevant information on precipitation

occurrence. At the same time, when only considering the snow-rain labels, the score increases to 0.9, indicating that this channel provides a significant discriminative power for precipitation phase detection. Now the question is why the water vapor channel 183 GHz provides more relevant mutual information with precipitation phase change than the known ice scattering channels at 89 and 166 GHz (Bennartz and Petty 2001; Bennartz and Bauer 2003). Findings by You et al. (2017) can provide an explanation.

In summary, the precipitation phase detection accuracy depends on the discriminative power of the channel in separating the high-frequency scattering signals of snowfall from the surface under the masking effects of water vapor emission. It was found that the 183±3 channel is the most sensitive channel to ice scattering in a relatively dry atmosphere while it remains fully agnostic to the land surface emissivity changes. As the water vapor increases to a moderate level, channel 183±7 becomes more sensitive to ice and snowfall scattering than other channels. However, in a very moist atmosphere with a relatively large amount of water vapor, the sensitivity of 166v to the surface emissivity drops markedly and the channel becomes more effective in capturing the ice and snowfall scattering. The MRMR results show that over the ocean, where the atmosphere is expected to be relatively wetter than land, the 183±7 channel provides higher mutual information with the precipitation type than 183±3 and vice versa. The 166v channel is the next most important high-frequency channel for precipitation phase detection over land and ocean.

2) Partial dependence analyses

Figure. 7 shows the partial dependence plots for the detection step (solid lines) and conditional observational probabilities (markers) for a few selected input variables using the test data. Over the ocean, as the 10h and 37h channels warm up, the probability of rainfall occurrence increases, explaining that the ML captures the raindrop and cloud liquid water emission signals for rainfall detection. The 10h GHz channel appears to provide specificity for rainfall detection with a probability greater than 0.5 across the analyzed range. Since the probabilities are almost the same for clear-sky and snowfall events, this channel does not provide any information for the snowfall detection, expectedly. While the probability increases monotonically with the temperature at 37h GHz, the PD analysis indicates that this channel is only effective for rainfall detection when the TBs are greater than 180 K.

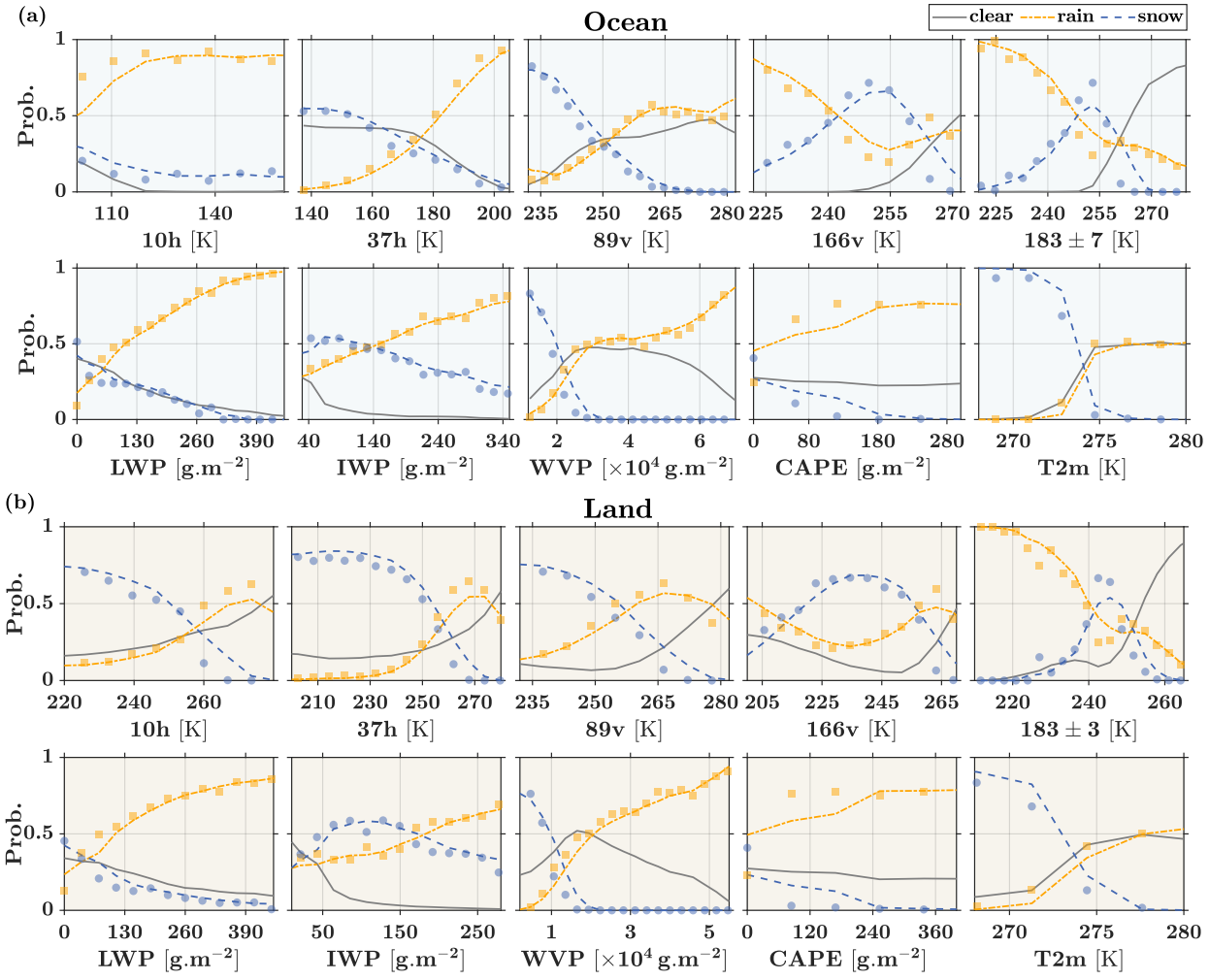

FIG. 7. Partial dependence analysis of the detection step using XGBDT for the test data over the ocean (top two rows) and land (bottom two rows). The analysis is confined to each bin to avoid sampling the low-probability regions of the joint distribution.

Among the scattering channels over the ocean, 89v shows high specificity in surface snowfall detection for TBs smaller than 250 K with no substantial information about rainfall detection. However, surprisingly, the 166v (183±7) channel with cold TBs below 240 (245) K is chiefly associated with high rainfall class probabilities and seems important only for snowfall detection over the range 240–265 (245–260) K with no discriminative power over warmer values. The results unravel that the coldest TBs in 89 (166) GHz are associated with snowfall (rainfall). One reason is that the 89 GHz channel responds to near-surface snowfall scattering; however,

higher frequencies capture the ice-aloft scattering (Skofronick-Jackson and Johnson 2011) that can statistically represent frequent heavy rainfall events in tall clouds with melting layers.

As the cloud IWP and LWP increase and the atmosphere becomes wetter over oceans, the ML produces higher rainfall class probability, and the surface snowfall is largely associated with drier atmospheric conditions. The PD of precipitation classes with CAPE is also consistent with the fact that rainfall events are more associated with strong convective activities than snowfall. The PD analysis of the 2-m air temperatures is striking and demonstrates how the used ML model can consistently capture the phase change of surface precipitation as a function of temperature.

Overland, the cold 10h and 37h TBs are associated with surface snowfall and do not provide any specificity for rainfall detection. These high snowfall class probabilities represent surrogate dependencies with the surface temperature and are unrelated to any scattering signatures, as discussed previously. The response patterns for high-frequency channels are similar to those over the ocean; however, these channels seem to provide more discriminative power, especially at 89 GHz.

3) Orbital retrievals

Figure 8 shows the result of ShARP^{ML} for GMI orbit #3080 over Greenland on September 13, 2014. Precipitation retrieval over an ice sheet is challenging because fewer active/passive coincidences exist over this specific surface type. Moreover, over a low emissive snow-covered ice, snowfall high-frequency scattering signatures can be weak and masked by supercooled cloud liquid water content.

Visual inspection of the 37 GHz channel (Fig. 8a–c) indicates a warming signal and thus a potential rainfall event over the North Atlantic Ocean and Greenland Strait. This warm signal is accompanied by cooling in both 89 and 166 GHz – indicating ice aloft scattering and occurrence of a melting layer. A warming signal is observed at 37 GHz, over the ice-free southern and western coastlines, covered with sub-arctic and tundra climate regimes. Perceptual interpretation of high-frequency TBs is not straightforward due to the complexity of radiometric interactions of snow-covered ice with atmospheric signals – especially at surface sensitive 89 GHz. Nevertheless, a cooling signal, likely due to ice particles and falling snow, is visible over the southwest coastlines at 166 GHz.

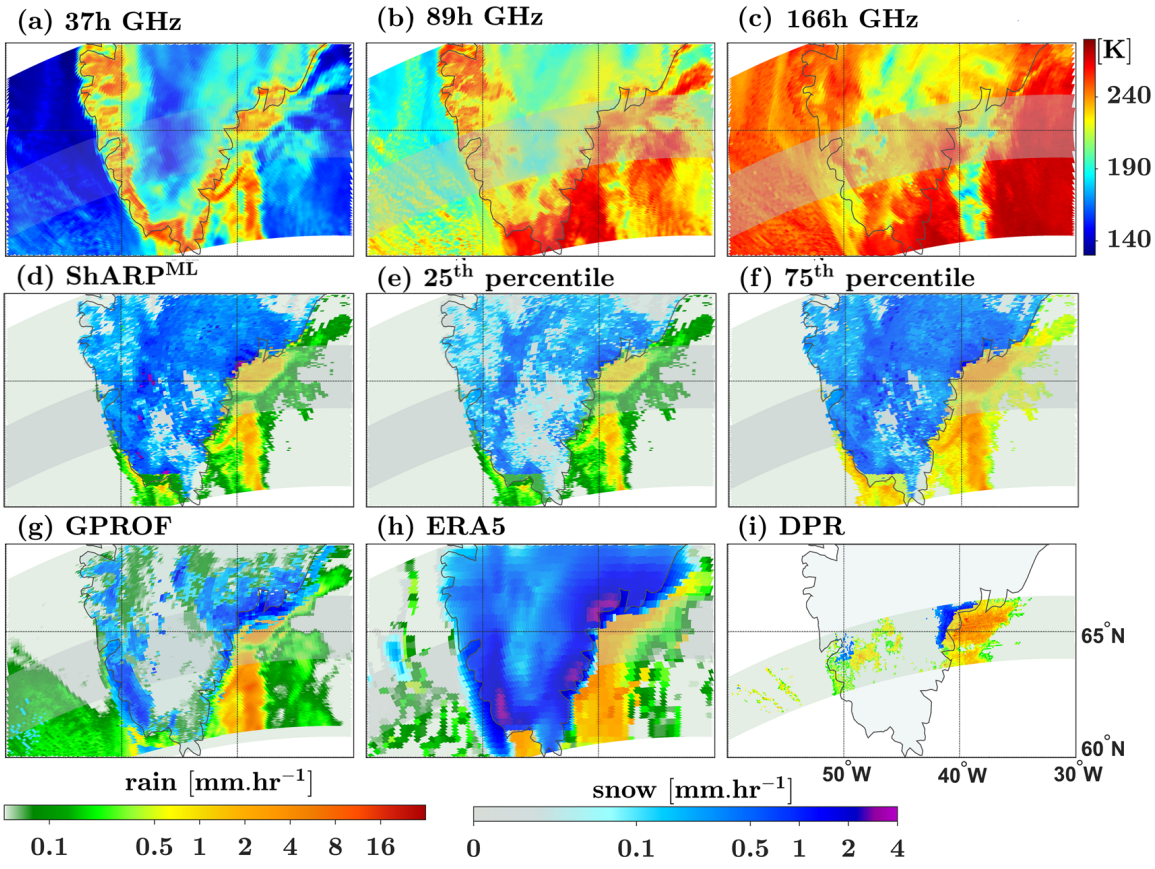

FIG. 8. Brightness temperatures by GMI (a–c), precipitation retrievals by ShARP^{ML} and its uncertainties (d–f) and precipitation from GPROF, ERA5, and DPR (g–i) for orbit #3080 on September 13, 2014 over Greenland.

The precipitation retrievals and ERA5 data (Fig. 8d–i) indicate that as the storm moves over the ice sheet, the phase of precipitation transitions from liquid to solid; however, they are notably different in the middle of the ice sheet. The ShARP^{ML}, which relies on CPR coincidences, shows a notable snowstorm covering the ice sheet consistent with the ERA5 data (Fig. 8h), even though the retrieved intensities are much lower. The retrieval quantiles indicate that the uncertainties are high and the distribution of the retrievals is wide in the middle of the storm. It is important to recall that ERA5 simulations represent a temporal interpolation between hourly simulations and are not instantaneous.

We also retrieve the extent and rate of a snowstorm near the coast of the Labrador Peninsula on January 3, 2019 – where CPR intersects the GMI orbit #27551 (Fig. 9). The narrow, sheared columnar-like CPR reflectivity profile (Fig. 9a), distributed across this cross-section with values

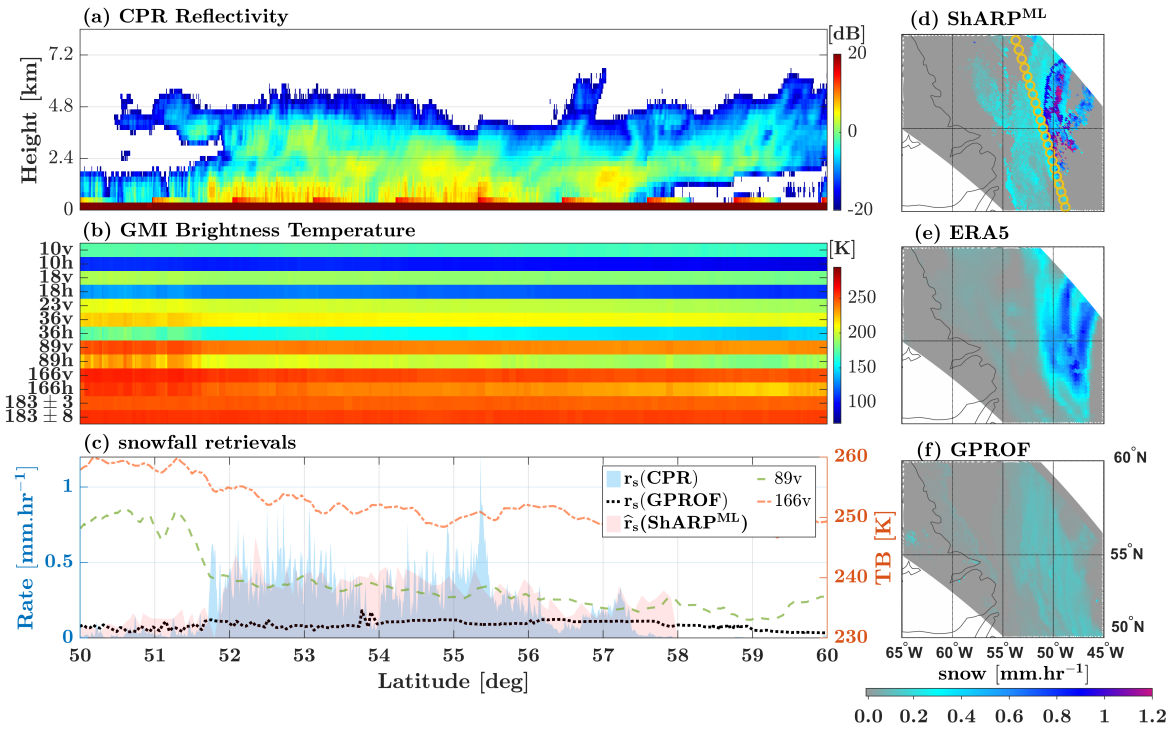

FIG. 9. Passive retrievals of a snowstorm captured by GPM orbit #27551 over the Labrador Sea on the west coast of Quebec in Canada on January 3, 2019. (a) The CPR reflectivity profile, (b) GMI TBs, (c) snowfall rates from CPR ($\mathbf{r_s}$, blue shaded area), ShARP^{ML} ($\hat{\mathbf{r}}_\mathbf{s}$, red solid line), GPROF ($\mathbf{r_s}$, black dotted line), and variation of TBs at channels 89v (green dashed line) and 166v GHz (orange dashed line) over the CPR track. The spatial representations are (d) ShARP^{ML}, (e) ERA5, and (f) GPROF retrievals on the GMI swath.

exceeding 10 dBZ to almost 2 km above the surface, indicates the occurrence of a moderately deep snowfall event. The TBs capture the scattering signatures from the shallow ice particles at 89 and 166 GHz (Fig. 9b), despite highly polarized surface emissivity over this intersection. These channels become colder by more than 10–15 K, as CPR moves toward the storm's northern edge with higher snowfall rates. Consistent with these scattering signatures, the CPR retrieves sporadic snowfall cells with a rate <1 mm hr^{-1}, while both GPROF and ShARP^{ML} retrieve lower rates than CPR. The ERA5 simulations represent the occurrence of a cohesive snowstorm with a rate of less than 0.75 mm hr^{-1}. Once again, we need to emphasize that there is a 15 min time lag between the CPR and GMI coincidences, and ERA5 snowfall is temporally interpolated.

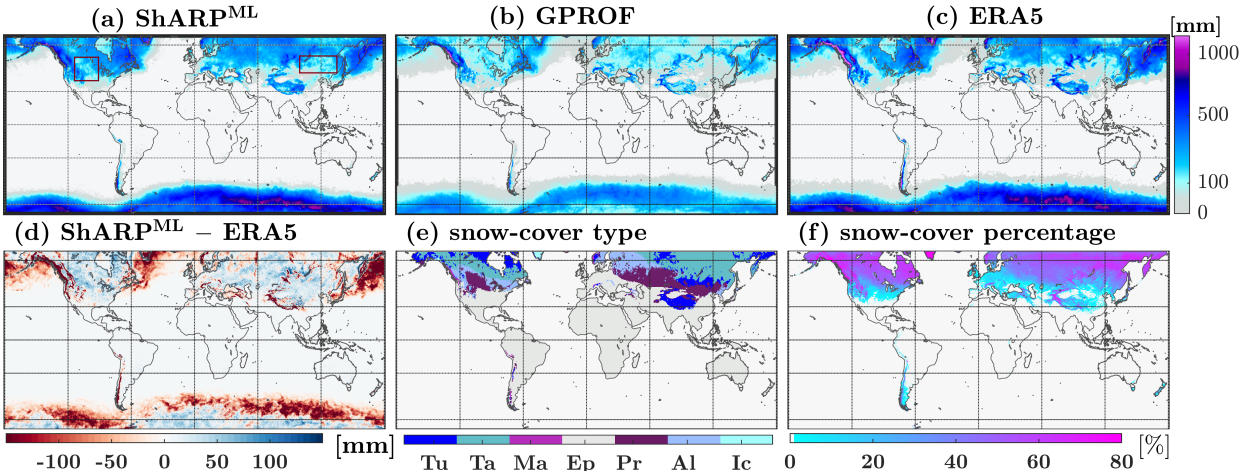

FIG. 10. Annual estimates of the total snowfall in 2022 at a 0.1-deg grid for (a) ShARP^{ML}, (b) GPROF, (c) ERA5, (d) the difference between ShARP^{ML} and ERA5 with (e) the snow cover classes include tundra (Tu), taiga (Ta), maritime (Ma), ephemeral (Ep), prairie (Pr), alpine (Al), and ice (Ic) as well as the (f) the annual MODIS snow-cover percentage.

e. Global Retrievals

An estimate of total annual snowfall in 2022 for all data products is shown in Fig. 10 on a 0.1-deg grid. The results suggest that GPROF underestimates snowfall over oceans compared to other retrievals consistent with previous findings (Skofronick-Jackson et al. 2019). The spatial patterns between ShARP^{ML} and ERA5 are in reasonable agreement over oceanic storm tracks in the Southern Ocean, the Bering Sea, and the Labrador Sea. However, it appears that over relatively ice-free (ice-covered) oceans, ShARP^{ML} tends to underestimate (overestimate) ERA5. It is well understood that the scattering signal of dry snow-covered sea ice can decrease the high-frequency TBs (Ebtehaj and Kummerow 2017; Vahedizade et al. 2021) and lead to some overestimation.

Notable differences are observed over terrestrial surfaces, especially in mountainous and low-land snow- and ice-covered areas. To provide additional insights on these differences, the annual snow-cover type (Sturm and Liston 2021) and fraction (Pagano and Durham 1993) from the Moderate Resolution Imaging Spectroradiometer (MODIS) are also shown in Figs. 10e,f. Overall, visual inspection indicates that ShARP^{ML} is prone to overestimate ERA5 over lowlands and underestimate it over mountainous regions and Greenland. The underestimation is more significant in GPROF than ShARP^{ML}, except over the Canadian Coast Mountains, where the orographic snowfall is the

dominant regime. However, compared to GPROF, the CPR-based retrievals are in better agreement with the reanalysis in other mountain ranges with predominantly orographic snowfall – such as the Norwegian mountains, the Himalayas, and the European and Japanese Alps. The underestimation of mountainous (orographic) snowfall is attributed to the fact that spaceborne retrievals can miss backscattered snowfall signatures over rough surfaces (Tang et al. 2017; Takbiri et al. 2019; Skofronick-Jackson et al. 2019). Moreover, due to the shallow nature of orographic snowfall, the snowfall passive scattering signatures can be markedly weak, especially over frequencies above 150 GHz that capture upper-level ice scattering (Skofronick-Jackson and Johnson 2011).

Over the temperate grasslands, savannas, and shrublands biomes in the Eurasian Steppe, where relatively shallow Prairie and Tundra snow cover are expected, GPROF (ShARP^{ML}) consistently underestimates (overestimates) ERA5. The climatological observations from the GlobSnow dataset (Takala et al. 2011) indicate that the mean annual snow depth varies from 200 (south) to 400 mm (north) in this ecoregion (Bormann et al. 2018), which seems to be consistent with the annual retrievals by ERA5 and ShARP^{ML}. The MODIS snow-cover percentage data (Fig. 10f) indicates that perhaps ShARP^{ML} is prone to overestimation over the Canadian Prairies and northeast China, marked with red boxes. These areas are often covered with seasonal shallow Prairie snow-cover type, which was recognized to manifest a similar scattering signal to snowfall (Rahimi et al. 2022) when the emerging vegetation is light and the snow depth is less than 15 cm.

The global snowfall retrievals of ShARP^{ML} (Fig. 10) are shown versus the ERA5 data over ocean and land in Fig. 11. The two data sets are more correlated over the ocean than over land. The ShARP^{ML} slightly underestimates (overestimates) the ERA5 over the ocean (land) by -30 (15) mm year^{-1}. The underestimation over oceans is largely accumulated where the total snowfall is less than 200 mm year^{-1} while for the higher accumulation rates 200–400 mm year^{-1}, satellite retrievals overestimate the reanalysis. On the contrary, the retrievals consistently overestimate ERA5 snowfall over land surfaces across a wide accumulation range of 0–400 mm year^{-1} (Fig. 11b).

The terrestrial differences and correlation values are further stratified and reported in Tab. 3. Consistent with spatial differences (Fig. 10d), the largest overestimation (underestimation) is over prairie (maritime) 23 (-32) mm year^{-1} snow types as well as ice-covered Greenland. The correlation between ShARP^{ML} and ERA5 snowfall data varies across snow types. The retrievals over ephemeral snow show the least discrepancy and highest correlations, where the likelihood of scat-

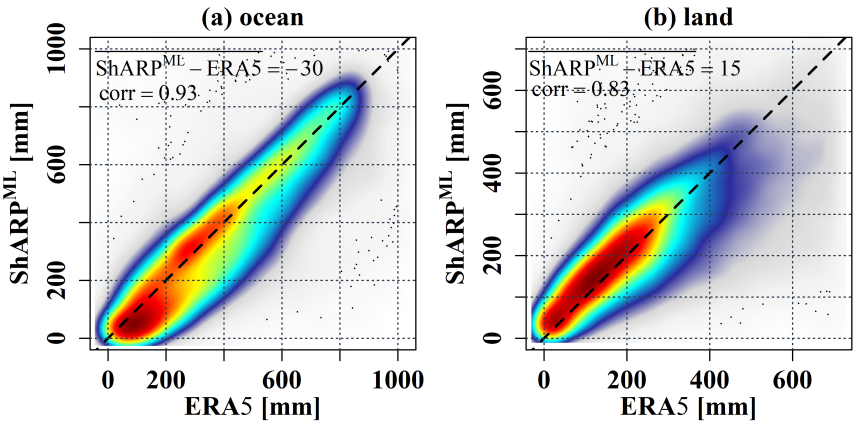

FIG. 11. Density scatter plots of annual snowfall from ShARP^{ML} and ERA5 (Fig. 10) over (a) ocean and (b) land at a 0.1-deg grid. Hot (red) and cold (blue) colors denote the higher and lower densities of the available data pairs. The corr denotes the correlation coefficient, and bias is reported in mm year^{-1}.

TABLE 3. Mean difference and correlation of annual ShARP^{ML} and ERA5 snowfall over different snow-cover types as explained in Fig. 10.

Snow types	Tu	Ta	Ma	Ep	Pr	Al	Ic
ShARP^{ML} - ERA5 [mm]	15	-3	-32	3	23	7	-25
Correlation Coef. (corr)	0.73	0.80	0.80	0.83	0.81	0.75	0.63

tering interference is minimal, as physically explained by Rahimi et al. (2022). High correlations in maritime (0.80) environment suggest that ShARP^{ML} and ERA5's spatial patterns are close in this regime despite the existing differences in the mean values. On the other hand, the lowest correlation is over ice-covered surfaces.

Overall, the zonal mean of snowfall retrievals (Fig. 12) shows that ShARP^{ML} and ERA5 retrievals are in latitudinal agreements despite reported spatial heterogeneity and differences. Over oceans, underestimation of ShARP^{ML} increases over polar latitudes, probably due to additional complexities of surface emissivity caused by heterogeneous sea ice variability in space and time. The agreement is stronger in the Southern Ocean, which makes up, on average, 80% of total oceanic snowfall. Over the Northern Hemispheric continents, there is a good agreement between zonal mean values, especially at 30–40°N. In the Southern Hemisphere, a significant difference between satellite

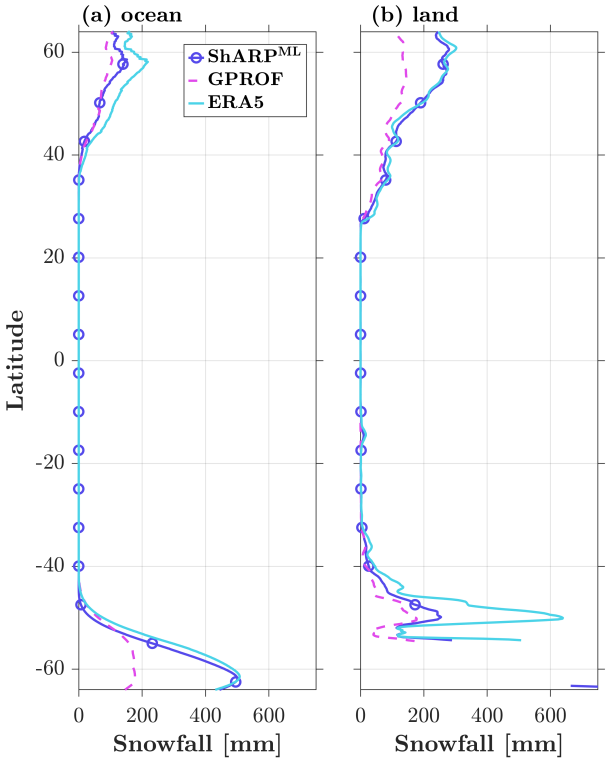

FIG. 12. Annual zonal mean of snowfall data over (a) ocean and (b) land obtained from Fig. 10.

retrievals and reanalysis data is observed over the Andes Mountains, perhaps indicating the lack of signal in coincidences used for the algorithm training.

5. Summary and Concluding Remarks

The paper proposed and studied the performance of a PMW precipitation retrieval pipeline that learns from coincidences of passive/active observations from the Global Precipitation Measurement (GPM) core satellite and the W-band CloudSat Profiling Radar (CPR) as ancillary reanalysis drivers of precipitation. This architecture first detects the precipitation, determines its phase through the XGBDT algorithm with weighted cross-entropy, and then estimates its rate through a Bayesian retrieval approach in the embedding space of a fully connected MLP, equipped with a focal loss function. Consistent with the previous literature (Rysman et al. 2018), we found that gradient-boosted decision trees can outperform multi-layer perceptions based on learning from the available CPR-GMI coincidences. We provided evidence suggesting that Bayesian retrievals in the embedding space of an MLP provide competitive and even higher-quality retrievals than the examined classic MLs. The results highlight the importance of using proper loss functions that can formally account for the imbalanced nature of the precipitation types and their skewed distributions.

A few research directions can be envisaged. The overestimation in snowfall retrievals over regions with shallow prairie snow was attributed to the similarity of snowfall and snow-cover scattering signals and requires further investigation. Due to a limited number of CPR observations and microwave frequency channels, resolving this ill-posedness might need additional ancillary data related to the physical characteristics of snow cover (i.e., thickness, density, and liquid water content) as well as information on vegetation water content perhaps from the Soil Moisture Active and Passive Satellite data (Kumawat et al. 2022; Kumawat and Ebtehaj 2023, 2024) over snow-covered surfaces.

The underestimation of snowfall in mountainous regions remains a challenge because of two main reasons. The sample size is small and lacks the backscattered signal of (shallow) orographic snowfall reflectivity due to increased surface roughness. Further constraining the retrievals using model simulations or reanalysis data might be inevitable when the scattering signal does not exist. Explainable machine learning can be further expanded to examine the signal strengths over complex terrains and the consistency of retrievals. Lastly, we need to emphasize that while visual comparisons with the GPROF product were provided, objective analysis will be needed to quantify

when, where, and to what extent the GMI-CPR coincidences can improve the retrievals globally, contingent upon the used algorithms.

Acknowledgments. The support from NASA's Remote Sensing Theory program (RST, 80NSSC20K1717), Making Earth System Data Records for Use in Research (MEaSUREs, 80NSSC24M0048) through Dr. Lucia Tsaoussi, and Global Precipitation Measurement (PMM, 80NSSC22K0596) through Dr. Will McCarty are acknowledged. Moreover, the authors acknowledge the Minnesota Supercomputing Institute (MSI) at the University of Minnesota for providing resources that contributed to the research results reported in this paper (https://www.msi.umn.edu/). A demo code that demonstrates the implementation of the algorithm is available at https://github.com/reyhaneh-92/Sharp_ML/tree/main.

Data availability statement. The datasets utilized in this study are openly accessible to the public. The GPM dataset can be downloaded from NASA's Global Precipitation Measurement (GPM) website at https://storm.pps.eosdis.nasa.gov/storm/data/Service.jsp?serviceName=Order. The ERA5 dataset is available for download through the Copernicus Climate Data Store (CDS) at https://cds.climate.copernicus.eu/cdsapp#!/dataset/reanalysis-era5-single-levels?tab=form.

References

Adrià Amell, Simon Pfreundschuh, and Patrick Eriksson. The chalmers cloud ice climatology: Retrieval implementation and validation. *Atmospheric Measurement Techniques*, 17:4337–4368, 7 2024. ISSN 18678548. doi: 10.5194/AMT-17-4337-2024.

P. M. Atkinson and A. R. L. Tatnall. Introduction neural networks in remote sensing. *International Journal of Remote Sensing*, 18:699–709, 3 1997. ISSN 0143-1161. doi: 10.1080/014311697218700.

Takumi Bannai, Haoyang Xu, Nobuyuki Utsumi, Eunho Koo, Keming Lu, and Hyungjun Kim. Multi-Task Learning for Simultaneous Retrievals of Passive Microwave Precipitation Estimates and Rain/No-Rain Classification. *Geophysical Research Letters*, 50(7):e2022GL102283, 2023.

Ali Behrangi, Matthew Christensen, Mark Richardson, Matthew Lebsock, Graeme Stephens, George J. Huffman, David Bolvin, Robert F. Adler, Alex Gardner, Bjorn Lambrigtsen, and Eric Fetzer. Status of high-latitude precipitation estimates from observations and reanalyses. *Journal of Geophysical Research: Atmospheres*, 121(9):4468–4486, 2016. ISSN 21698996. doi: 10.1002/2015JD024546.

Ralf Bennartz and Peter Bauer. Sensitivity of microwave radiances at 85-183 GHz to precipitating ice particles. *Radio Science*, 38(4), 2003. ISSN 00486604. doi: 10.1029/2002RS002626. URL http://doi.wiley.com/10.1029/2002RS002626.

Ralf Bennartz and Grant W. Petty. The sensitivity of microwave remote sensing observations of precipitation to ice particle size distributions. *Journal of Applied Meteorology*, 40:345–364, 2001. ISSN 0894-8763. doi: 10.1175/1520-0450(2001)040⟨0345:TSOMRS⟩2.0.CO;2.

James Bergstra and Yoshua Bengio. Random search for hyper-parameter optimization. *Journal of machine learning research*, 13(2), 2012.

Vadim Borisov, Tobias Leemann, Kathrin Sebler, Johannes Haug, Martin Pawelczyk, and Gjergji Kasneci. Deep neural networks and tabular data: A survey. *IEEE Transactions on Neural Networks and Learning Systems*, 35:7499–7519, 6 2024. ISSN 21622388. doi: 10.1109/TNNLS.2022.3229161.

Kat J Bormann, Ross D Brown, Chris Derksen, and Thomas H Painter. Estimating snow-cover trends from space. *Nature Climate Change*, 8(11):924–928, 2018.

Leo Breiman. Random forests. *Machine learning*, 45:5–32, 2001.

Daniele Casella, Giulia Panegrossi, Paolo Sanò, Anna Cinzia Marra, Stefano Dietrich, Benjamin T. Johnson, and Mark S. Kulie. Evaluation of the GPM-DPR snowfall detection capability: Comparison with CloudSat-CPR. *Atmospheric Research*, 2017. ISSN 01698095. doi: 10.1016/j.atmosres.2017.06.018.

Tianqi Chen and Carlos Guestrin. Xgboost: A scalable tree boosting system. In *Proceedings of the 22nd acm sigkdd international conference on knowledge discovery and data mining*, pages 785–794, 2016.

T. M. Cover and P. E. Hart. Nearest Neighbor Pattern Classification. *IEEE Transactions on Information Theory*, 1967. ISSN 15579654. doi: 10.1109/TIT.1967.1053964.

Ardeshir Ebtehaj and Christian Kummerow. Microwave retrievals of terrestrial precipitation over snow-covered surfaces: A lesson from the GPM satellite. *Geophysical Research Letters*, 6 2017. ISSN 00948276. doi: 10.1002/2017GL073451. URL http://doi.wiley.com/10.1002/2017GL073451.

Ardeshir Ebtehaj, Rafael L. Bras, and Efi Foufoula-Georgiou. Shrunken Locally Linear Embedding for Passive Microwave Retrieval of Precipitation. *IEEE Transactions on Geoscience and Remote Sensing*, 53(7):3720–3736, 2015. ISSN 01962892. doi: 10.1109/TGRS.2014.2382436.

Ardeshir Ebtehaj, Christian D Kummerow, and F Joseph Turk. Metric Learning for Approximatio. *IEEE Transactions on Geoscience and Remote Sensing*, 58(2), 2020. ISSN 15580644. doi: 10.1109/TGRS.2019.2941682.

Ardeshir M Ebtehaj, Rafael L Bras, and Efi Foufoula-Georgiou. Evaluation of ShARP passive rainfall retrievals over snow-covered land surfaces and coastal zones. *Journal of Hydrometeorology*, 17(4), 2016. ISSN 15257541. doi: 10.1175/JHM-D-15-0164.1.

Kaushik Gopalan, Nai-Yu Yu Wang, Ralph Ferraro, Chuntao Liu, Kaushik Gopalan, Nai-Yu Yu Wang, Ralph Ferraro, and Chuntao Liu. Status of the TRMM 2A12 land precipitation algorithm.

Journal of Atmospheric and Oceanic Technology, 27(8):1343–1354, 8 2010. ISSN 07390572. doi: 10.1175/2010JTECHA1454.1.

Vesta Afzali Gorooh, Ata Akbari Asanjan, Phu Nguyen, Kuolin Hsu, and Soroosh Sorooshian. Deep neural network high spatiotemporal resolution precipitation estimation (deep-step) using passive microwave and infrared data. *Journal of Hydrometeorology*, 2 2022. ISSN 1525-755X. doi: 10.1175/JHM-D-21-0194.1.

Mircea Grecu, William S Olson, Stephen Joseph Munchak, Sarah Ringerud, Liang Liao, Ziad Haddad, Bartie L Kelley, and Steven F McLaughlin. The gpm combined algorithm. *Journal of Atmospheric and Oceanic Technology*, 33:2225–2245, 10 2016. ISSN 0739-0572. doi: 10.1175/JTECH-D-16-0019.1. URL https://journals.ametsoc.org/view/journals/atot/33/10/jtech-d-16-0019_1.xml.

Norman C. Grody. Classification of snow cover and precipitation using the special sensor microwave imager. *Journal of Geophysical Research*, 96(D4):7423, 1991. ISSN 0148-0227. doi: 10.1029/91JD00045.

Atsushi Hamada and Yukari N Takayabu. Improvements in detection of light precipitation with the global precipitation measurement dual-frequency precipitation radar (gpm dpr). *Journal of Atmospheric and Oceanic Technology*, 33:653–667, 2016. doi: 10.1175/JTECH-D-15-0097.1. URL https://journals.ametsoc.org/view/journals/atot/33/4/jtech-d-15-0097_1.xml.

Trevor Hastie, Robert Tibshirani, and Jerome Friedman. The Elements of Statistical Learning. *Elements*, 1:337–387, 2009. ISSN 03436993. doi: 10.1007/b94608. URL http://www.springerlink.com/index/10.1007/b94608.

John M. Haynes, Tristan S. L'Ecuyer, Graeme L. Stephens, Steven D. Miller, Cristian Mitrescu, Norman B. Wood, and Simone Tanelli. Rainfall retrieval over the ocean with spaceborne W-band radar. *Journal of Geophysical Research Atmospheres*, 2009. ISSN 01480227. doi: 10.1029/2008JD009973.

Kaiming He, Xiangyu Zhang, Shaoqing Ren, and Jian Sun. Deep residual learning for image recognition. 2016. URL http://image-net.org/challenges/LSVRC/2015/.

Hans Hersbach, Bill Bell, Paul Berrisford, Shoji Hirahara, András Horányi, Joaquín Muñoz-Sabater, Julien Nicolas, Carole Peubey, Raluca Radu, Dinand Schepers, Adrian Simmons, Cornel Soci, Saleh Abdalla, Xavier Abellan, Gianpaolo Balsamo, Peter Bechtold, Gionata Biavati, Jean Bidlot, Massimo Bonavita, Giovanna Chiara, Per Dahlgren, Dick Dee, Michail Diamantakis, Rossana Dragani, Johannes Flemming, Richard Forbes, Manuel Fuentes, Alan Geer, Leo Haimberger, Sean Healy, Robin J. Hogan, Elías Hólm, Marta Janisková, Sarah Keeley, Patrick Laloyaux, Philippe Lopez, Cristina Lupu, Gabor Radnoti, Patricia Rosnay, Iryna Rozum, Freja Vamborg, Sebastien Villaume, and Jean-Noël Thépaut. Era5 hourly data on single levels from 1979 to present. copernicus climate change service (c3s) climate data store (cds). (accessed on 03-2021). 2018. doi: 10.24381/cds.adbb2d47.

Masafumi Hirose, Shoichi Shige, Takuji Kubota, Fumie A. Furuzawa, Haruya Minda, and Hirohiko Masunaga. Refinement of surface precipitation estimates for the dual-frequency precipitation radar on the gpm core observatory using near-nadir measurements. *Journal of the Meteorological Society of Japan. Ser. II*, 99:1231–1252, 10 2021. ISSN 0026-1165. doi: 10.2151/JMSJ.2021-060.

TRH Holmes, RAM De Jeu, M Owe, and AJ Dolman. Land surface temperature from Ka band (37 GHz) passive microwave observations. *Journal of Geophysical Research: Atmospheres*, 114 (D4), 2009.

Toshio Iguchi, Toshiaki Kozu, Robert Meneghini, Jun Awaka, and Ken'ichi Okamoto. Rain-Profiling Algorithm for the TRMM Precipitation Radar. *Journal of Applied Meteorology*, 39 (12):2038–2052, 2000. ISSN 0894-8763. doi: 10.1175/1520-0450(2001)040⟨2038:RPAFTT⟩2.0.CO;2.

Toshio Iguchi, Shinta Seto, Robert Meneghini, Naofumi Yoshida, Jun Awaka, and Takuji Kubota. Gpm / dpr level-2 algorithm theoretical basis document. 2018. URL https://gpm.nasa.gov/sites/default/files/2019-05/ATBD_DPR_201811_with_Appendix3b.pdf.

Min-Jeong Jeong Kim, J. A. Weinman, W. S. Olson, D.-E. E. Chang, G. Skofronick-Jackson, and J. R. Wang. A physical model to estimate snowfall over land using AMSU-B observations. *Journal of Geophysical Research Atmospheres*, 113(9):D09201, 5 2008. ISSN 01480227. doi: 10.1029/2007JD008589.

Diederik P. Kingma and Jimmy Lei Ba. Adam: A Method for Stochastic Optimization. *3rd International Conference on Learning Representations, ICLR 2015 - Conference Track Proceedings*, 12 2014. doi: 10.48550/arxiv.1412.6980. URL https://arxiv.org/abs/1412.6980v9.

Cezar Kongoli, Paul Pellegrino, Ralph R. Ferraro, Norman C. Grody, and Huan Meng. A new snowfall detection algorithm over land using measurements from the Advanced Microwave Sounding Unit (AMSU). *Geophysical Research Letters*, 30(14):n/a–n/a, 7 2003. ISSN 00948276. doi: 10.1029/2003GL017177. URL http://doi.wiley.com/10.1029/2003GL017177.

Cezar Kongoli, Huan Meng, Jun Dong, and Ralph Ferraro. A snowfall detection algorithm over land utilizing high-frequency passive microwave measurements - Application to ATMS. *Journal of Geophysical Research Atmospheres*, 120(5):1918–1932, 2015. ISSN 21698996. doi: 10.1002/2014JD022427.

Mark S. Kulie, Ralf Bennartz, Thomas J. Greenwald, Yong Chen, and Fuzhong Weng. Uncertainties in Microwave Properties of Frozen Precipitation: Implications for Remote Sensing and Data Assimilation. *Journal of the Atmospheric Sciences*, 67(11):3471–3487, 2010. ISSN 0022-4928. doi: 10.1175/2010JAS3520.1.

Divya Kumawat and Ardeshir Ebtehaj. Passive microwave retrieval of vegetation optical depth and soil permittivity over snow covered surfaces at l-band. *International Geoscience and Remote Sensing Symposium (IGARSS)*, 2023-July:3241–3244, 2023. doi: 10.1109/IGARSS52108.2023.10282460.

Divya Kumawat and Ardeshir Ebtehaj. Deep learning of the soil freeze-thaw cycle using satellite l-band radiometry. pages 3218–3221, 9 2024. doi: 10.1109/IGARSS53475.2024.10641878.

Divya Kumawat, Mohammadali Olyaei, Lun Gao, and Ardeshir Ebtehaj. Passive microwave retrieval of soil moisture below snowpack at l-band using smap observations. *IEEE Transactions on Geoscience and Remote Sensing*, page 1, 2022. doi: 10.1109/TGRS.2022.3216324.

Christian Kumerrow. Gpm gmi (gprof) radiometer precipitation profiling l2a 1.5 hours 13 km v05. *Greenbelt, MD, Goddard Earth Sciences Data and Information Services Center (GES DISC)*, 2016.

Christian Kummerow, William S. Olson, and Louis Giglio. A simplified scheme for obtaining precipitation and vertical hydrometeor profiles from passive microwave sensors. *IEEE Transactions on Geoscience and Remote Sensing*, 34(5):1213–1232, 1996. ISSN 01962892. doi: 10.1109/36.536538.

Christian Kummerow, Y. Hong, W. S. Olson, S. Yang, R. F. Adler, J. McCollum, R. Ferraro, G. Petty, D-B. Shin, and T. T. Wilheit. The Evolution of the Goddard Profiling Algorithm (GPROF) for Rainfall Estimation from Passive Microwave Sensors. *Journal of Applied Meteorology*, 40(11): 1801–1820, 2001. ISSN 0894-8763. doi: 10.1175/1520-0450(2001)040⟨1801:TEOTGP⟩2.0.CO;2.

Christian D. Kummerow and Louis Giglio. A Passive Microwave Technique for Estimating Rainfall and Vertical Structure Information from Space. Part I: Algorithm Description, 1994. ISSN 0894-8763. URL http://journals.ametsoc.org/doi/abs/10.1175/1520-0450(1994)033<0003:APMTFE>2.0.CO;2.

Christian D Kummerow, David L Randel, Mark Kulie, Nai-Yu Wang, Ralph Ferraro, S Joseph Munchak, and Veljko Petkovic. {T}he {E}volution of the {G}oddard {P}rofiling {A}lgorithm to a {F}ully {P}arametric {S}cheme. *J. Atmos. Oceanic Technol.*, 2015. ISSN 0739-0572. doi: 10.1175/JTECH-D-15-0039.1. URL http://dx.doi.org/10.1175/JTECH-D-15-0039.1.

Tristan S Lécuyer and Graeme L Stephens. {A}n uncertainty model for {B}ayesian {M}onte {C}arlo retrieval algorithms: {A}pplication to the {TRMM} observing system. *Quart. J. Roy. Meteor. Soc.*, 128(583):1713–1737, 2002. ISSN 1477-870X. doi: 10.1002/qj.200212858316. URL http://dx.doi.org/10.1002/qj.200212858316.

Guosheng Liu. Deriving snow cloud characteristics from cloudsat observations. *Journal of Geophysical Research: Atmospheres*, 113(D8), 2008.

Guosheng Liu and Judith A Curry. Retrieval of precipitation from satellite microwave measurement using both emission and scattering. *Journal of Geophysical Research: Atmospheres*, 97(D9): 9959–9974, 1992. ISSN 2156-2202. doi: 10.1029/92JD00289. URL http://dx.doi.org/10.1029/92JD00289.

Guosheng Liu and Eun-Kyoung Seo. Detecting snowfall over land by satellite high-frequency microwave observations: The lack of scattering signature and a statistical approach. *Journal of Geophysical Research: Atmospheres*, 118(3):1376–1387, 2 2013. ISSN 2169897X. doi: 10.1002/jgrd.50172. URL http://doi.wiley.com/10.1002/jgrd.50172.

Sergey Y. Matrosov and Alessandro Battaglia. Influence of multiple scattering on cloudsat measurements in snow: A model study. *Geophysical Research Letters*, 36:L12806, 6 2009. ISSN 0094-8276. doi: 10.1029/2009GL038704.

Jeffrey R McCollum and Ralph R Ferraro. Next generation of NOAA/NESDIS TMI, SSM/I, and AMSR-E microwave land rainfall algorithms. *Journal of Geophysical Research: Atmospheres*, 108(D8), 2003. ISSN 2156-2202. doi: 10.1029/2001JD001512. URL http://dx.doi.org/10.1029/2001JD001512.

Huan Meng, Jun Dong, Ralph Ferraro, Banghua Yan, Limin Zhao, Cezar Kongoli, Nai Yu Wang, and Bradley Zavodsky. A 1DVAR-based snowfall rate retrieval algorithm for passive microwave radiometers. *Journal of Geophysical Research: Atmospheres*, 122 (12):6520–6540, 6 2017. ISSN 2169-8996. doi: 10.1002/2016JD026325. URL https://onlinelibrary.wiley.com/doi/full/10.1002/2016JD026325https://onlinelibrary.wiley.com/doi/abs/10.1002/2016JD026325https://agupubs.onlinelibrary.wiley.com/doi/10.1002/2016JD026325.

Lisa Milani, Mark S. Kulie, Daniele Casella, Stefano Dietrich, Tristan S. L'Ecuyer, Giulia Panegrossi, Federico Porcù, Paolo Sanò, and Norman B. Wood. CloudSat snowfall estimates over Antarctica and the Southern Ocean: An assessment of independent retrieval methodologies and multi-year snowfall analysis. *Atmospheric Research*, 2018. ISSN 01698095. doi: 10.1016/j.atmosres.2018.05.015.

Lisa Milani, Mark S. Kulie, Daniele Casella, Pierre E. Kirstetter, Giulia Panegrossi, Veljko Petkovic, Sarah E. Ringerud, Jean Franqois Rysman, Paolo Sano, Nai Yu Wang, Yalei You, and Gail Skofronick-Jackson. Extreme Lake-Effect Snow from a GPM Microwave Imager Perspective: Observational Analysis and Precipitation Retrieval Evaluation. *Journal of Atmospheric and Oceanic Technology*, 38(2):293–311, 2 2021. ISSN 0739-0572. doi:

798 10.1175/JTECH-D-20-0064.1. URL https://journals.ametsoc.org/view/journals/
799 atot/38/2/JTECH-D-20-0064.1.xml.

800 S Joseph Munchak and Gail Skofronick-Jackson. Evaluation of precipitation detection over various
801 surfaces from passive microwave imagers and sounders. *Atmospheric Research*, 131:81–94,
802 2013.

803 Yoo-Jeong Noh, Guosheng Liu, Eun-Kyoung Seo, James R. Wang, and Kazumasa Aonashi. Devel-
804 opment of a snowfall retrieval algorithm at high microwave frequencies. *Journal of Geophysical*
805 *Research*, 111(D22):D22216, 11 2006. ISSN 0148-0227. doi: 10.1029/2005JD006826. URL
806 http://doi.wiley.com/10.1029/2005JD006826.

807 Christopher W. O'Dell, Frank J. Wentz, and Ralf Bennartz. Cloud liquid water path from satellite-
808 based passive microwave observations: A new climatology over the global oceans. *Journal of*
809 *Climate*, 2008. ISSN 08948755. doi: 10.1175/2007JCLI1958.1.

810 William S Olson. Physical retrieval of rainfall rates over the ocean by multispectral microwave
811 radiometry: Application to tropical cyclones. *J. Geophys. Res.*, 94(D2):2267–2280, 1989.
812 ISSN 2156-2202. doi: 10.1029/JD094iD02p02267. URL http://dx.doi.org/10.1029/
813 JD094iD02p02267.

814 Marko Orescanin, Veljko Petković, Scott W Powell, Benjamin R Marsh, and Sean C Heslin.
815 Bayesian deep learning for passive microwave precipitation type detection. *IEEE Geoscience*
816 *and Remote Sensing Letters*, 19:1–5, 2021.

817 Thomas S Pagano and Rodney M Durham. Moderate resolution imaging spectroradiometer
818 (MODIS). In *Sensor Systems for the Early Earth Observing System Platforms*, volume 1939,
819 pages 2–17. SPIE, 1993.

820 Hanchuan Peng, Fuhui Long, and Chris Ding. Feature selection based on mutual information
821 criteria of max-dependency, max-relevance, and min-redundancy. *IEEE Transactions on pattern*
822 *analysis and machine intelligence*, 27(8):1226–1238, 2005.

823 Grant W Petty. Physical retrievals of over-ocean rain rate from multichannel microwave im-
824 agery. Part II: Algorithm implementation. *Meteorology and Atmospheric Physics*, 1994. ISSN
825 01777971. doi: 10.1007/BF01030054.

Grant W Petty and Ke Li. Improved Passive Microwave Retrievals of Rain Rate over Land and Ocean. Part I: Algorithm Description. *Journal of Atmospheric and Oceanic Technology*, 30 (11):2493 – 2508, 2013. doi: https://doi.org/10.1175/JTECH-D-12-00144.1. URL https://journals.ametsoc.org/view/journals/atot/30/11/jtech-d-12-00144_1.xml.

Simon Pfreundschuh, Paula J. Brown, Christian D. Kummerow, Patrick Eriksson, and Teodor Norrestad. GPROF-NN: A neural-network-based implementation of the Goddard Profiling Algorithm. *Atmospheric Measurement Techniques*, 15(17):5033–5060, 9 2022. ISSN 18678548. doi: 10.5194/AMT-15-5033-2022.

Reyhaneh Rahimi, Ardeshir Ebtehaj, Giulia Panegrossi, Lisa Milani, Sarah E. Ringerud, and F. Joseph Turk. Vulnerability of Passive Microwave Snowfall Retrievals to Physical Properties of Snowpack: A Perspective From Dense Media Radiative Transfer Theory. *IEEE Transactions on Geoscience and Remote Sensing*, 60, 2022. ISSN 15580644. doi: 10.1109/TGRS.2022.3184530.

Olaf Ronneberger, Philipp Fischer, and Thomas Brox. U-net: Convolutional networks for biomedical image segmentation. *Lecture Notes in Computer Science (including subseries Lecture Notes in Artificial Intelligence and Lecture Notes in Bioinformatics)*, 9351:234–241, 2015. ISSN 16113349. doi: 10.1007/978-3-319-24574-4{_}28/COVER. URL https://link.springer.com/chapter/10.1007/978-3-319-24574-4_28.

Jean François Rysman, Giulia Panegrossi, Paolo Sanò, Anna Cinzia Marra, Stefano Dietrich, Lisa Milani, and Mark S. Kulie. SLALOM: An all-surface snow water path retrieval algorithm for the GPM microwave imager. *Remote Sensing*, 2018. ISSN 20724292. doi: 10.3390/rs10081278.

Jean François Rysman, Giulia Panegrossi, Paolo Sanò, Anna Cinzia Marra, Stefano Dietrich, Lisa Milani, Mark S. Kulie, Daniele Casella, Andrea Camplani, Chantal Claud, and Léo Edel. Retrieving Surface Snowfall With the GPM Microwave Imager: A New Module for the SLALOM Algorithm. *Geophysical Research Letters*, 46(22): 13593–13601, 11 2019. ISSN 1944-8007. doi: 10.1029/2019GL084576. URL https://onlinelibrary.wiley.com/doi/full/10.1029/2019GL084576https://onlinelibrary.wiley.com/doi/abs/10.1029/2019GL084576https://agupubs.onlinelibrary.wiley.com/doi/10.1029/2019GL084576.

Paolo Sanò, Giulia Panegrossi, Daniele Casella, Anna Marra, Leo D'Adderio, Jean Rysman, and Stefano Dietrich. The passive microwave neural network precipitation retrieval (pnpr) algorithm for the conical scanning global microwave imager (gmi) radiometer. *Remote Sensing*, 10: 1122, 7 2018. ISSN 2072-4292. doi: 10.3390/rs10071122. URL http://www.mdpi.com/2072-4292/10/7/1122.

Riku Shimizu, Shoichi Shige, Toshio Iguchi, Cheng-Ku Yu, and Lin-Wen Cheng. Narrowing the blind zone of the gpm dual-frequency precipitation radar to improve shallow precipitation detection in mountainous areas. *Journal of Applied Meteorology and Climatology*, 62(10): 1437–1450, 2023.

Gail Skofronick-Jackson and Benjamin T. Johnson. Surface and atmospheric contributions to passive microwave brightness temperatures for falling snow events. *Journal of Geophysical Research: Atmospheres*, 116(D2), 1 2011. ISSN 2156-2202. doi: 10.1029/2010JD014438. URL https://onlinelibrary.wiley.com/doi/full/10.1029/2010JD014438https://onlinelibrary.wiley.com/doi/abs/10.1029/2010JD014438https://agupubs.onlinelibrary.wiley.com/doi/10.1029/2010JD014438.

Gail Skofronick-Jackson, Walter A. Petersen, Wesley Berg, Chris Kidd, Erich F. Stocker, Dalia B. Kirschbaum, Ramesh Kakar, Scott A. Braun, George J. Huffman, Toshio Iguchi, Pierre E. Kirstetter, Christian Kummerow, Robert Meneghini, Riko Oki, William S. Olson, Yukari N. Takayabu, Kinji Furukawa, and Thomas Wilheit. The global precipitation measurement (GPM) mission for science and Society. *Bulletin of the American Meteorological Society*, 2017. doi: 10.1175/BAMS-D-15-00306.1.

Gail Skofronick-Jackson, Mark Kulie, Lisa Milani, Stephen J Munchak, Norman B Wood, and Vincenzo Levizzani. Satellite estimation of falling snow: A global precipitation measurement (GPM) core observatory perspective. *Journal of applied meteorology and climatology*, 58(7): 1429–1448, 2019.

Gail M. Skofronick-Jackson, James A. Weinman, Min Jeong Kim, and Dong Eon Chang. A physical model to determine snowfall over land by microwave radiometry. *IEEE Transactions on Geoscience and Remote Sensing*, 42(5):1047–1058, 2004. ISSN 01962892. doi: 10.1109/TGRS.2004.825585.

Gail M. Skofronick-Jackson, Benjamin T. Johnson, and S. Joseph Munchak. Detection thresholds of falling snow from satellite-borne active and passive sensors. *IEEE Transactions on Geoscience and Remote Sensing*, 51:4177–4189, 7 2013. ISSN 0196-2892. doi: 10.1109/TGRS.2012.2227763.

Graeme L. Stephens, Deborah G. Vane, Simone Tanelli, Eastwood Im, Stephen Durden, Mark Rokey, Don Reinke, Philip Partain, Gerald G. Mace, Richard Austin, Tristan L'Ecuyer, John Haynes, Matthew Lebsock, Kentaroh Suzuki, Duane Waliser, Dong Wu, Jen Kay, Andrew Gettelman, Zhien Wang, and Rojer Marchand. CloudSat mission: Performance and early science after the first year of operation. *Journal of Geophysical Research Atmospheres*, 2009. ISSN 01480227. doi: 10.1029/2008JD009982.

Matthew Sturm and Glen E Liston. Revisiting the global seasonal snow classification: An updated dataset for earth system applications. *Journal of Hydrometeorology*, 22(11):2917–2938, 2021.

Matias Takala, Kari Luojus, Jouni Pulliainen, Chris Derksen, Juha Lemmetyinen, Juha-Petri Kärnä, Jarkko Koskinen, and Bojan Bojkov. Estimating northern hemisphere snow water equivalent for climate research through assimilation of space-borne radiometer data and ground-based measurements. *Remote Sensing of Environment*, 115(12):3517–3529, 2011.

Zeinab Takbiri, Ardeshir Ebtehaj, Efi Foufoula-Georgiou, Pierre-Emmanuel Kirstetter, and F Joseph Turk. A prognostic nested k-nearest approach for microwave precipitation phase detection over snow cover. *Journal of hydrometeorology*, 20(2):251–274, 2019.

Guoqiang Tang, Yixin Wen, Jinyu Gao, Di Long, Yingzhao Ma, Wei Wan, and Yang Hong. Similarities and differences between three coexisting spaceborne radars in global rainfall and snowfall estimation. *Water Resources Research*, 53:3835–3853, 5 2017. ISSN 00431397. doi: 10.1002/2016WR019961. URL http://doi.wiley.com/10.1002/2016WR019961.

Guoqiang Tang, Di Long, Ali Behrangi, Cunguang Wang, and Yang Hong. Exploring deep neural networks to retrieve rain and snow in high latitudes using multisensor and reanalysis data. *Water Resources Research*, 54:8253–8278, 10 2018. ISSN 0043-1397. doi: 10.1029/2018WR023830. URL https://onlinelibrary.wiley.com/doi/abs/10.1029/2018WR023830.

F. J. Tapiador, C. Kidd, K. L. Hsu, and F. Marzano. Neural networks in satellite rainfall estimation. *Meteorological Applications*, 11:83–91, 3 2004. ISSN 1469-8080. doi: 10.1017/S1350482704001173.

James W. Taylor. A quantile regression neural network approach to estimating the conditional density of multiperiod returns. *Journal of Forecasting*, 19:299 – 311, 7 2000. ISSN 02776693. doi: 10.1002/1099-131x(200007)19:4⟨299::aid-for775⟩3.3.co;2-m.

F J Turk, Sarah E Ringerud, Andrea Camplani, Daniele Casella, Randy J Chase, Ardeshir Ebtehaj, Jie Gong, Mark Kulie, Guosheng Liu, Lisa Milani, Giulia Panegrossi, Ramon Padullés, Jean-François Rysman, Paolo Sanò, Sajad Vahedizade, and Norman B Wood. Applications of a cloudsat-trmm and cloudsat-gpm satellite coincidence dataset. *Remote Sensing*, 13, 2021. doi: 10.3390/rs13122264.

Sajad Vahedizade, Ardeshir Ebtehaj, Yalei You, Sarah E. Ringerud, and F. Joseph Turk. Passive microwave signatures and retrieval of high-latitude snowfall over open oceans and sea ice: Insights from coincidences of gpm and cloudsat satellites. *IEEE Transactions on Geoscience and Remote Sensing*, 2021. ISSN 15580644. doi: 10.1109/TGRS.2021.3071709.

Chen Wang, Chengyuan Deng, and Suzhen Wang. Imbalance-XGBoost: Leveraging weighted and focal losses for binary label-imbalanced classification with XGBoost. *Pattern Recognition Letters*, 136:190–197, August 2020. ISSN 0167-8655. doi: 10.1016/j.patrec.2020.05.035.

T T Wilheit, A T C Chang, M S V. Rao, E B Rodgers, and J S Theon. Satellite Technique for Quantitatively Mapping Rainfall Rates over the Oceans. *J. Appl. Meteor.*, 16(5):551–560, 5 1977. ISSN 0021-8952. doi: 10.1175/1520-0450(1977)016⟨0551:ASTFQM⟩2.0.CO;2.

N. B. Wood, T. S. L'Ecuyer, F. L. Bliven, and G. L. Stephens. Characterization of video disdrometer uncertainties and impacts on estimates of snowfall rate and radar reflectivity. *Atmospheric Measurement Techniques*, 2013. ISSN 18671381. doi: 10.5194/amt-6-3635-2013.

Norman B. Wood, Tristan S. L'Ecuyer, Andrew J. Heymsfield, Graeme L. Stephens, David R. Hudak, and Peter Rodriguez. Estimating snow microphysical properties using collocated multisensor observations. *Journal of Geophysical Research Atmospheres*, 119(14):8941–8961, 2014. ISSN 21698996. doi: 10.1002/2013JD021303.

Yalei You, Nai-Yu Wang, Ralph Ferraro, and Scott Rudlosky. Quantifying the snowfall detection performance of the GPM Microwave Imager channels over land. *Journal of Hydrometeorology*, 18(3):729–751, 2017.

Yalei You, Huan Meng, Jun Dong, Yongzhen Fan, Ralph R. Ferraro, Guojun Gu, and Likun Wang. A Snowfall Detection Algorithm for ATMS Over Ocean, Sea Ice, and Coast. *IEEE Journal of Selected Topics in Applied Earth Observations and Remote Sensing*, 15:1411–1420, 2022. ISSN 21511535. doi: 10.1109/JSTARS.2022.3140768.

Yalei You, George Huffman, Veljko Petkovic, Lisa Milani, John X. Yang, Ardeshir Ebtehaj, Sajad Vahedizade, and Guojun Gu. Evaluation of snowfall retrieval performance of gpm constellation radiometers relative to spaceborne radars. *Journal of Hydrometeorology*, 24:389–405, 3 2023. ISSN 1525-7541. doi: 10.1175/JHM-D-22-0052.1. URL https://journals.ametsoc.org/view/journals/hydr/24/3/JHM-D-22-0052.1.xml.